JGR Earth Surface

RESEARCH ARTICLE
10.1029/2024JF008255

Progressive Development of a Paraglacial Rock Slope Failure at Portage Glacier, Alaska

Emilie Lemaire[1], Jane Walden[2,3], Bretwood Higman[4], Anja Dufresne[1], Pooya Hamdi[1], Andrea Manconi[5,6], Mylène Jacquemart[2,3], and Florian Amann[1,7]

[1]RWTH-Aachen University, Institute of Engineering Geology and Hydrogeology, Aachen, Germany, [2]Laboratory of Hydraulics, Hydrology and Glaciology, ETH Zürich, Zürich, Switzerland, [3]Swiss Federal Institute for Forest, Snow and Landscape Research (WSL), Sion, Switzerland, [4]Ground Truth Alaska, Seldovia, AK, USA, [5]WSL Institute for Snow and Avalanche Research SLF, Davos Dorf, Switzerland, [6]Climate Change, Extremes and Natural Hazards in Alpine Regions Research Centre CERC, Davos Dorf, Switzerland, [7]Fraunhofer Research Institution for Energy Infrastructures and Geotechnologies IEG, Aachen, Germany

Abstract Paraglacial landscapes are rapidly transforming as thinning and retreating glaciers expose adjacent slopes to new conditions. In Southcentral Alaska, a large slope instability at Portage Glacier has been deforming progressively up-glacier over the past six decades. The instability comprises two deep-seated rock slope segments, Portage A and Portage B, located above the thinning and retreating Portage Glacier and its proglacial lake. Portage B lies at the glacier terminus, while the down-glacier margin of Portage A is about 300 m further up-glacier. To understand the mechanisms driving slope deformation, we integrated field observations, historical imagery, structural and kinematic analysis, differential DEMs, InSAR, and coherence radar to capture both short- and long-term deformation patterns. We identified three distinct domains of movement: two in Portage A and one in Portage B. Our findings reveal that Portage A experiences rapid and variable displacement rates, whereas Portage B shows slower motion. Structural analysis indicates translational sliding and toppling as primary failure mechanisms controlled by pre-existing geological discontinuities. Glacier thinning is identified as a key factor, initiating movement and enabling the progressive spatial up-glacier propagation of deformation from Portage B to Portage A. But this process is not solely driven by thinning; rather, it reflects how ice loss progressively alters mechanical boundary conditions, granting kinematic freedom for the rock mass to deform along pre-existing structural discontinuities. Consequently, our results underscore the importance of considering both glacier thickness thresholds and structural geology to better understand and assess the onset and evolution of slope deformation in paraglacial environments.

Plain Language Summary As glaciers get thinner and retreat, the surrounding landscape changes quickly. In south-central Alaska, near Portage Glacier, a large unstable slope has been moving over six decades. The slope has two unstable areas: Portage A, farther up-glacier, and Portage B, near the current glacier terminus. To understand how glacier thinning and retreat influence slope movement, we used field observations, historical images, elevation change analysis, and advanced radar techniques to track movement over time. Our analysis revealed three movement zones: two in Portage A and one in Portage B. Portage A shows faster and more variable motion, while Portage B moves more slowly and consistently. The main causes of this movement are sliding and toppling along natural rock fractures. Glacier thinning plays a major role, as reduced ice support allows deformation to spread up-glacier from Portage B to Portage A. However, thinning alone does not fully explain the observed deformation. The gradual ice loss changes the physical forces holding the slope in place, allowing rock to move along existing weaknesses. This study highlights the combined importance of glacier thickness and the geologic features in shaping the timing and pattern of slope movement in places where glaciers are retreating and thinning.

Key Points:

- Contemporary glacier retreat causes vertical and lateral progressive rock slope failure at Portage Glacier, Alaska
- Structural pre-conditioning is the key factor controlling progressive paraglacial failure evolution
- Failure initiates at a glacier thickness threshold

Supporting Information:

Supporting Information may be found in the online version of this article.

Correspondence to:

E. Lemaire,
lemaire@lih.rwth-aachen.de

Citation:

Lemaire, E., Walden, J., Higman, B., Dufresne, A., Hamdi, P., Manconi, A., et al. (2025). Progressive development of a paraglacial rock slope failure at Portage Glacier, Alaska. *Journal of Geophysical Research: Earth Surface*, *130*, e2024JF008255. https://doi.org/10.1029/2024JF008255

Received 3 JAN 2025
Accepted 8 NOV 2025

Author Contributions:

Conceptualization: Emilie Lemaire, Bretwood Higman, Anja Dufresne, Pooya Hamdi, Florian Amann
Funding acquisition: Anja Dufresne, Pooya Hamdi, Florian Amann
Investigation: Emilie Lemaire, Jane Walden, Bretwood Higman, Anja Dufresne, Pooya Hamdi
Validation: Andrea Manconi, Mylène Jacquemart
Visualization: Emilie Lemaire
Writing – original draft: Emilie Lemaire
Writing – review & editing: Jane Walden, Bretwood Higman, Anja Dufresne, Pooya Hamdi, Andrea Manconi, Mylène Jacquemart, Florian Amann

1. Introduction

The stability of alpine slopes is influenced by a complex interplay of factors, including the removal of glacier ice (e.g., Ballantyne, 2002; Dai et al., 2020; Grämiger et al., 2017; Kos et al., 2016; Lacroix et al., 2022), seismic activity (e.g., Gorum et al., 2011; Keefer, 1984; Marc et al., 2015), climatic forces (e.g., Chen and Lee, 2003; Dahal and Hasegawa, 2008; Iverson, 2000), and permafrost degradation (e.g., Darrow et al., 2024; Etzelmüller et al., 2022; Huggel et al., 2010; Patton et al., 2021). If a slope is susceptible to these factors due to its unfavorable

geological or morphological preconditioning, rock damage may initiate and accumulate over time, gradually reducing the slope's stability.

In paraglacial environments, the interaction between glacier dynamics and slope stability has become a prominent research topic (e.g., Augustinus, 1995; Ballantyne, 2002; Coe et al., 2018; Donati et al., 2023; Evans & Clague, 1994; Higman et al., 2018; Hugentobler et al., 2022; Huggel et al., 2012; Kos et al., 2016; Lemaire et al., 2024; McColl, 2012; Oppikofer et al., 2008; Rechberger et al., 2021). Paraglacial mass movements are defined by slope failure occurring in regions undergoing a transition from glacial to non-glacial conditions (McColl, 2012; Slaymaker, 2009; Storni et al., 2020). Glacier retreat may play a significant role in slope stability modifications in paraglacial environments, where the landscape morphology and a variety of coupled physical processes (e.g., glacial erosion, hydrothermal cycling, stress redistribution) are influenced by past glacier cycles and ongoing deglaciation. As glaciers recede, they often expose over-steepened rock slopes, increasing the potential for more frequent rock falls and, depending on the geological settings, deep-seated landslides (Ballantyne, 2002; Ben-Yehoshua et al., 2022; Huggel et al., 2012; Klimeš et al., 2021; Lacroix et al., 2022; McColl, 2012; McColl & Davies, 2013; Oppikofer et al., 2008).

Glacier thinning and retreat results in unloading of bedrock and stress redistribution, which can lead to rock slope destabilization in case of unfavorable geological conditions (McColl, 2012). However, the direct connection between glacier retreat and slope stability remains not fully understood due to the diverse failure mechanisms and timing of slope failures observed in different contexts. On one hand, the findings of Storni et al. (2020), show that glaciers may influence the speed of landslide movements, but their overall impact on slope stability is minimal. Additionally, Grämiger et al. (2017) used advanced numerical models and showed that for the Moosfluh landslide in Switzerland, repeated thermal and hydraulic stress variations caused by glaciation cycles gradually damage rock formations, and these stress variations better explain the development of rock slope deformation as compared to debuttressing. Both of these studies, suggest that the glacier has only a limited impact on rock slope stability, and other factors may be more important. On the other hand, Kos et al. (2016) evaluated long-term monitoring data of the Moosfluh landslide and found that after the ice thickness at the toe of the moving landslide reached a critical thickness, a major acceleration phase was triggered. Lacroix et al. (2022) further support this notion by demonstrating that during periods of rapid glacier mass loss, significant acceleration of landslide movement can occur. These examples suggest that the glacier does exert some control over the rock slope dynamics. However, despite the potential impact of glacier retreat and cyclic variations on rock slope stability, many paraglacial rock slopes exposed to the dynamics of a retreating and thinning glacier remain stable. Although glacial unloading affects nearly all formerly glaciated valleys, Bovis (1982) and Ballantyne (2002) emphasized that deep-seated deformations are spatially limited. Thus, independent factors, such as the geological composition, structural setting (i.e., kinematic freedom), strength and stiffness of the rock mass and discontinuities, degree of fracturing, and geomorphological features of the slopes are equally crucial in assessing and understanding the spatial and temporal development of rock slope instabilities and the involved volume. In this paper, the term instability refers to the section of the slope that has experienced or/and continues to exhibit movement, typically bounded by a main scarp, but has not yet undergone complete slope failure.

In paraglacial environments, progressive failure represents a fundamental mechanism in the long-term evolution of rock slope stability. In this study, we conceptualize progressive failure as occurring in two primary modes:

- Temporal progression, involving the gradual accumulation of damage over time; and
- Spatial progression, involving the spatial extension of failure once initiated.

Temporal progression refers to a gradual mechanical weakening of the slope over time, in which subcritical damage accumulates progressively within the rock mass or along structural discontinuities. This degradation is strongly influenced by preconditioning factors such as the lithology and the tectonic heritage of the rock mass. Time-dependent failures are often driven by a combination of environmental factors such as weathering, glacial unloading, seismic activity, and hydrological fluctuations (e.g., Eberhardt et al., 2017; Grämiger et al., 2017; McColl & Davies, 2013; Riva et al., 2018; Voigtländer, 2020). Over time, these processes progressively reduce the rock mass strength, eventually leading to critical deformation and failure. Spatial progression occurs once a failure has initiated and subsequently extends across the slope, either laterally or vertically. Slope failure may not occur as a single event; it can also evolve progressively in space depending on structural and kinematic conditions, geomorphological aspects of the slope, and other environmental factors. This spatial progression can unfold over timescales ranging from days to decades.

A considerable amount of research has emerged focusing on paraglacial slope instabilities, often relying on retrospective analyses of historical case studies using remote sensing data (e.g., Deline et al., 2015; Lemaire et al., 2024; Oppikofer et al., 2008). Due to the difficulty of collecting sufficiently detailed field data in remote alpine environments, with active deglaciation and slope deformation (Storni et al., 2020), only few studies succeeded to reconstruct the longer-term development of paraglacial rock slope instabilities based on both remote sensing and field data (e.g., Donati et al., 2023; Kos et al., 2016; Lemaire et al., 2024; Oppikofer et al., 2008; Storni et al., 2020).

In Alaska, paraglacial slope failure has gained attention as a growing hazard (e.g., Dai et al., 2020; Donati et al., 2023; Dufresne et al., 2019; Higman et al., 2018; Lemaire et al., 2024; Petley, 2022; Schaefer et al., 2024; Walden et al., 2025). Those adjacent to water bodies have the potential to trigger tsunamis, potentially causing significant damages with devastating impacts on humans, infrastructures, marine traffic, wildlife, and the natural environment (e.g., Higman et al., 2018; Miller, 1960; Wiles & Calkin, 1992).

Despite significant advances in understanding paraglacial slope processes worldwide, knowledge gaps remain in capturing and understanding the full spatio-temporal progressive evolution of slope deformation in response to glacier changes. This study addresses this gap by integrating a multi-disciplinary data set, including historical photographs, structural mapping, kinematic analysis, satellite-based interferometric synthetic aperture radar (InSAR), and aerial photogrammetry, to reconstruct the progressive slope response to ongoing deglaciation. Our research focuses on analyzing the spatial and temporal patterns of slope movement associated with glacier thinning at Portage Glacier in Southcentral Alaska, with the goal of understanding the factors driving slope deformation in a rapidly changing paraglacial environment. The studied rock slope is located adjacent to Portage Lake, posing a potential tsunami threat and thus highlighting the broader societal relevance of this research. Through a detailed back analysis of the progressive slope deformation and the glacier historical evolution, along with structural and kinematic assessment and high-resolution surface displacement monitoring of the slope instabilities, this study provides new insights into the long- and short-term progressive development of paraglacial slope failures under changing environmental conditions. This contributes to a better understanding of how slopes respond under the influence of glacial dynamics and climate variations, and provides the necessary evidence-based foundation for a quantitative hazard analysis, both through time and space.

2. Study Area

The study area is located within the Chugach National Forest on the Kenai Peninsula in Alaska (Figure 1). It is situated about 7 km west of Whittier, a small town, and about 90 km southeast of Anchorage, the largest city in Alaska. The area is dominated by Portage Glacier, a valley glacier that has undergone significant retreat and thinning in recent decades. Originating from an ice field at ∼1,430 m a.s.l., the glacier flows northeast, terminating in its proglacial lake at about 30 m a.s.l. Portage Glacier once filled the entire valley, that is now occupied by the proglacial lake, making it a vital transportation route for centuries. Prior to 1914, both Portage Glacier and Portage Pass were used to access the Passage Canal at Whittier (Mayo et al., 1977).

The studied instabilities are located on a mountain side referred to as Portage slope directly adjacent to Portage Glacier and its proglacial lake, and are referred to as Portage A and Portage B (Figure 1), following the naming convention established by Schaefer et al. (2024). These paraglacial slope instabilities are situated on a slope with an average inclination of ∼35°. Portage B, located at the glacier terminus, extends 350 m up-glacier and reaches a height of approximately 480 m. Directly up-glacier, Portage A spans a width of about 780 m, with its height ranging from ∼250 to ∼600 m, reflecting its distinctive triangular shape. The unstable areas show signs of active movement, including tension cracks, exposed bedrock, and accumulations of loose rock debris at the base of the slope. Previous studies showed that the slope experienced movement at both Portage A and Portage B (Schaefer et al., 2024; Walden et al., 2025).

These instabilities are of particular concern due to their potential hazard implications. The Begich, Boggs Visitor Center, situated on the terminal moraine left behind by Portage Glacier, is located only a couple meters above lake level. Portage Glacier and Lake are favored tourist attractions, drawing crowds of visitors year-round. During the busy summer season, daily boat tours are offered to view the glacier from the lake (Figure 1). Additionally, a critical transportation tunnel, situated less than 1 km from Portage Lake, provides the only land- access to Whittier (Figure 1).

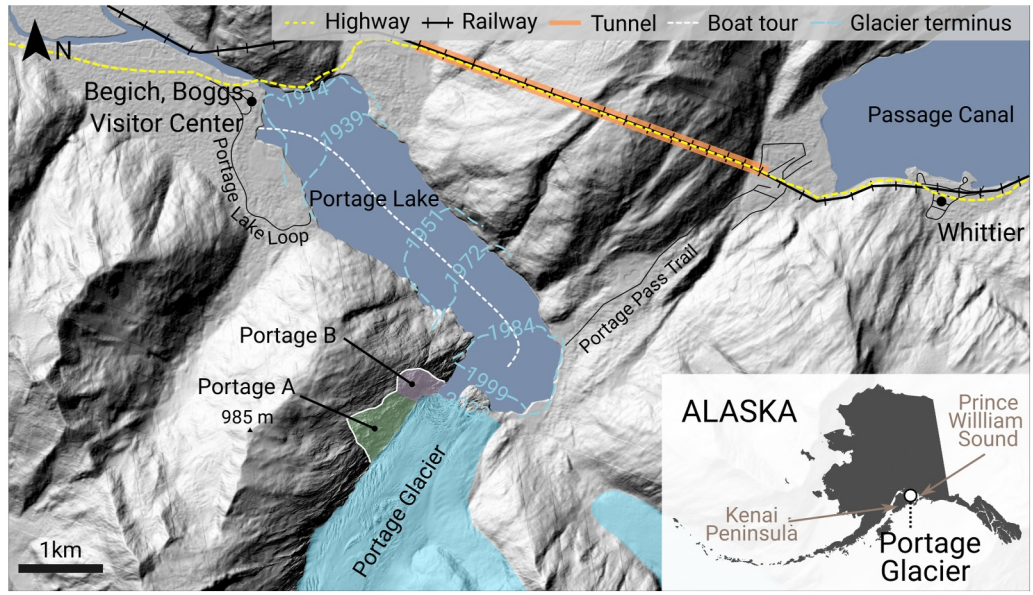

Figure 1. Overview map of the study area and the location of the site in Alaska. The background map is a hillshade derived from the 2014 IfSAR DEM product (downloaded from https://elevation.alaska.gov, accessed on 22 March 2022). The glacier terminus positions are based on Mayo et al. (1977).

2.1. Portage Glacier

Similar to most glaciers worldwide, Portage Glacier has undergone significant changes over the past centuries due to climate variations, with Alaska being a hotspot for rapid glacier retreat and contributing 25% of global glacier mass loss in the last decades (Hugonnet et al., 2021). Observations of Portage Glacier date back to the late 1700s (Mayo et al., 1977; Nistor & Petcu, 2014), with the advancement of Portage Glacier of about 5 km between 1794 and 1880–1990 (Mayo et al., 1977). However, around the mid-19th century, coincident with the climate-warming period at the end of the Little Ice Age, Portage Glacier started to retreat (Kennedy et al., 2006). Until the early 1900s, Portage Glacier filled the basin with ice and its terminus extended onto the land at the end of today's Portage Lake (Figure 1). The glacier began a noticeable retreat at the start of the 20th century and as the glacier continued to recede, it transitioned from being a land-terminating glacier to a lake-terminating glacier. While atmospheric warming initially drove the ice loss, this transition shifted the dominant mechanism of retreat to calving into the proglacial lake, which then became the primary driver of mass loss (Crossen, 2007; Kennedy et al., 2006). The calving process considerably accelerated the retreat of the glacier, leading to a rapid expansion of the lake (Kennedy et al., 2006). Between 1939 and 1950, the glacier underwent a rapid retreat phase where the terminus receded by approximately 140–160 m/yr (Kennedy et al., 2006). During this phase, the increasing water depth at the terminus, reaching around 200 m (Kennedy et al., 2006), likely played a significant role in amplifying the calving rate (Benn et al., 2007; Crossen, 2007) and further accelerating the glacier's retreat. Retreat slowed dramatically in the 1990s as the calving face retreated through shallower water and parts of exposed dry land. During the early 2000s, the glacier began to uncover a segment of bedrock in its central area, marking a shift in its retreat dynamics. This shift has been quantitatively analyzed by Walden et al. (2025), who found that between 1985 and 2000, the glacier retreated rapidly at a rate of around 65 m/yr, followed by a stable phase until 2015, after which the retreat rate increased to about 40 m/yr. Thinning rates also decreased over this period, with a rate of 2.2 m/yr before 2000, dropping to approximately 1.6 m/yr from 2000 to 2020 (Walden et al., 2025).

2.2. Geological Context

In 1939, the Alaska Railroad, in collaboration with the U.S. Geological Survey, conducted an extensive geological investigation of the region. The primary objective was to assess the feasibility of constructing a railroad connection to Whittier. The study found that the bedrock composition in the area is predominantly slate, argillite, and graywacke, forming part of the same extensive geological series that extends from the Kenai Peninsula into the Prince William Sound region (Barnes, 1943) (see Figure S1 in Supporting Information S1).

These rock formations are considered to be of at least Cretaceous age (Barnes, 1943). The area is composed of a thick sequence of altered sediments, characterized by a succession of irregularly layered mudstones and impure sandstones that have experienced significant deformation, including folding, faulting, and metamorphosing (Barnes, 1943). The bedding thickness varies widely, ranging from less than 2.5 cm to over 30 m (Barnes, 1943). Untangling this geological series poses significant challenges in the identification and recognition of key beds due to the absence of bed persistency, and the overall lithological uniformity of the series without continuous individual lithological units (Barnes, 1943). The bedding predominantly shows an orientation toward the northeast with a sub-vertical dip. Nevertheless, some parts of the area have been influenced by more extensive folding along steep axes oriented toward the northeast (Barnes, 1943). In addition, no large-scale faults have been documented near the study area.

2.3. Seismic Context

Situated on the Kenai Peninsula, which is known for its high seismic activity due to its location along the Aleutian-Alaska subduction zone (Li et al., 2013), the study area experiences significant seismic events. Since 1950, approximately 85 earthquakes with magnitudes greater than 4.5 have been recorded within a 100 km radius of Portage Glacier, along with 80 earthquakes exceeding magnitude 2.5 within a 30 km radius (U.S. Geological Survey, 2024). Portage lies near the surface projection of the rupture area of the second largest earthquake worldwide and the largest in North American history (M_W 9.2) that occurred on 27 March 1964 in Prince William Sound. The Modified Mercalli Intensity (MMI) of the 1964 Great Alaskan earthquake was estimated at 8 MMI in Whittier (U.S. Geological Survey, 2020).

2.4. Climate Context

The Portage area is characterized by a subarctic maritime climate influenced by its proximity to the Gulf of Alaska and the North Pacific Ocean. The mean annual air temperature from 2013 to 2023 was 3.7°C, with average summer temperatures ranging around 12°C and winter temperatures around −5°C (National Weather Service, 2024). Precipitation falls mainly as snow during winter due to low temperatures. In winter, the lake can freeze completely, and the surrounding slopes are covered in snow, with accumulations of a few meters. Water is thus stored at the surface and released through snowmelt in late spring and summer, generating groundwater recharge in the fractured bedrock and surface runoff. Several permafrost distribution models for Alaska, including those by Brown et al. (1997), Ferrians (1965), Jorgenson et al. (2008), and Pastick et al. (2015), suggest that permafrost is not present around the Portage Glacier area.

3. Methods and Data

3.1. Workflow and Data Set

This study followed the workflow shown in Figure 2, with a summary of all data presented in Table 1. First, a back-analysis was performed based on the analysis of available imagery and topographic data dating back to the 1950s, obtained from the USGS Earth Explorer database (https://earthexplorer.usgs.gov/, accessed on 09 October 2023). The aerial photographs were georeferenced with control points located in stable areas outside the zones of instability and adjusted with a polynomial or thin plate spline transformation to align the data set. Second, geomorphological and structural analysis were carried out during fieldwork campaigns in August 2022 and July 2023. Structural mapping and aerial helicopter-based aerial imagery supported the geomorphological characterization of the slope. Visible geomorphologic features such as bedrock, rock debris, surface cracks, tilting blocks, and waterfalls/gullies were mapped based on the photographs and digitized as polylines or polygons. Third, slope displacement analysis integrated DEMs, LiDAR, and SAR data. Long-term displacements (annual to multi-year), were derived from LiDAR (2015, 2020) and Structure from Motion (SfM) DEMs (2022, 2023), while InSAR and coherence SAR images provided higher temporal resolution (12, 24, or 36 days) but lower spatial resolution. Combining these complementary data sets with geomorphological observations allowed us to distinguish between shallow and deep-seated movements (dashed line in Figure 2). Together, these methods contribute to a better understanding of the slope kinematics.

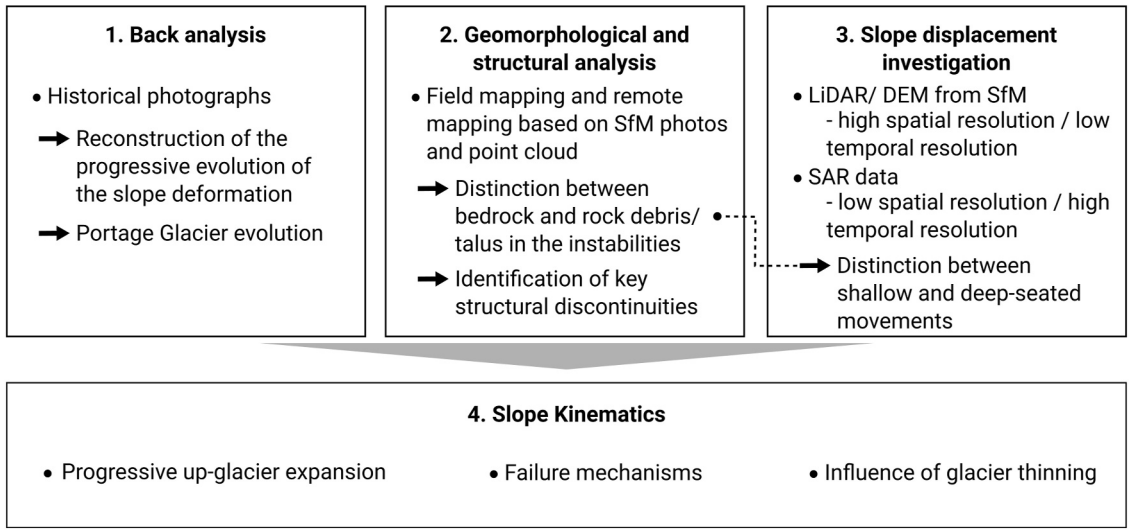

Figure 2. Research workflow for analyzing slope kinematics and failure mechanisms and the influence of glacier changes at the Portage slope. The dashed line indicates the input used from one step to the next one.

3.2. Structural Mapping and Kinematic Analysis

Structural mapping was conducted through a combination of field observations and remote sensing techniques. A total of 241 structural measurements were mapped within the Portage slope during both field campaigns using conventional structural mapping methods. These measurements were taken in stable bedrock areas outside the instabilities (see Figure S1 in Supporting Information S1). In addition to these conventional measurements, additional 123 structural measurements were obtained from the point cloud generated by the SfM method (see Section 3.3). This identification was carried out using the "Compass" tool in CloudCompare software (CloudCompare, 2023).

We analyzed various failure mechanisms, including planar sliding, flexural toppling, and wedge sliding, with respect to the orientation of the Portage slope. The kinematic method employed in our structural analysis assumes

Table 1
Database for Portage Glacier and Slope

Data set/source	Year(s)	Data type/method	Resolution (m)
NOAA Digital collections	1914	Photo	n.d.
USGS photos	1950	Aerial Photos	~1
	1964		
	1967		
	1968		
	1999	Digital orthophoto quadrangle	
	2006	High Resolution Orthoimagery	
ESRI Wayback imagery	2014	Maxar (WV02) image	~0.6
	2023		
Anchorage LiDAR DEM[a]	2015	Airborne LiDAR	0.9
Portage LiDAR[b]	2020		0.2
DEM (SfM)[c]	2022	Photogrammetry	~0.1
	2023		
SAR data	2015–2021	Ascending	2 in range 13 in azimuth
	2015–2023	Descending	

[a](OCM Partners, 2015). [b](Zechmann et al., 2024). [c](Lemaire, 2024).

that the discontinuities are fully persistent, dry, and cohesionless, while individual rock blocks are treated as rigid bodies (Wyllie & Mah, 2004). This analysis does not factor in lateral constraints or external forces acting on the blocks. We conducted a kinematic analysis for planar sliding, flexural toppling, and wedge failure. For planar sliding, we considered lateral limits deviating between 20° and 30° from the slope's dip direction (Wyllie & Mah, 2004). In the case of flexural toppling, the critical zone's lateral extents were set at a deviation of 20–30° from the slope's dip direction (Goodman, 1989). Wedge sliding failure is possible if the intersection of two joint planes dips at an angle lower than the slope angle and greater than the friction angle (Markland, 1972). Although we did not directly measure the shear strength of the discontinuities, a friction angle in the range of 25–30° was considered (Wyllie & Norrish, 1996).

3.3. Structure From Motion

Photogrammetric surveys were conducted during field campaigns on 10 August 2022 and 14 July 2023. In both campaigns, we followed the same acquisition process, ensuring consistency in our data collection. The photogrammetric surveys were done using Nikon D5600 and Canon EOS 850D cameras. The images were taken from a helicopter, with two individuals equipped with a camera capturing images that overlap by approximately 70%. These images were acquired from various angles and positions, ensuring coverage of the entire area of interest. In each campaign, approximately 2000 images were collected and processed using Agisoft Metashape (Agisoft Metashape, 2022) and the Structure from Motion (SfM) technique to generate 3D models of objects or landscapes from 2D images. We generated high-resolution 3D point clouds, digital elevation models (DEMs) and orthophotos of both the glacier and instabilities.

3.4. Surface Deformation

3.4.1. Digital Elevation Model Differencing

To accurately track the changes between the 2015, 2020, 2022, and 2023 DEMs (see Table 1), a precise alignment of these data sets is necessary. We achieved this by co-registering stable ground in the three data sets using the respective point clouds in the CloudCompare software. Parts of the slope that are known to be moving, as well as those that were snow-covered, are considered disruptive for the alignment and were thus excluded from the alignment. Therefore, we segmented each point cloud to isolate the stable part of the slope. The stable and snow-free segments from the 2015, 2020, 2022, and 2023 data sets were aligned using a transformation matrix, and this matrix was then applied uniformly to the entire unsegmented point cloud. Following the alignment process, the co-registered point clouds were converted into raster DEMs. The DEMs were imported into GIS software, where we used the raster calculator to compute the elevation differences between the 2015 and 2020 data sets, the 2020 and 2022 data sets, and the 2022 and 2023 data sets.

To assess the uncertainty, we applied the empirical uncertainty estimation method described by Miles et al. (2018), using the code provided by Jacquemart (2020). By systematically subdividing the DEM difference map into n^2 tiles, where n ranges from 2 to 200, the method calculates the mean absolute elevation difference within each tile as a measure of uncertainty. For this analysis, the stable slope portion of the map was used exclusively, excluding the glacier and moraine areas from the calculations. The resulting uncertainty estimates for DEM differencing (1.28 km^2) were as follows: 1 m ($n = 2$) to 1.9 m ($n = 200$) for the period 2015–2020, 0.04 m ($n = 2$) to 0.36 m ($n = 200$) for the period 2020–2022, and 0.04 m ($n = 2$) to 0.43 m ($n = 200$) for the period 2022–2023.

3.4.2. Displacement Analysis

To analyze the 3D displacement characteristics of the slope, we used Digital Image Correlation (DIC) with hillshade images generated from co-registered (see Section 3.4.1) 2020, 2022, and 2023 DEM data sets. Building on the DIC results and the DEMs, we performed further processing using Python.

We used the open-source software Ncorr (Blaber et al., 2015), specifically developed for DIC analysis. Ncorr employs a subset-based algorithm that divides the image into circular and contiguous subsets with the assumption of homogeneous deformations (Blaber & Antoniou, 2017). By tracking the displacement of these pixel subsets between two images, Ncorr quantifies deformation.

From the DIC results, we generated a 2D vector map, calculated the total displacement for each pixel, and determined the angle of the vertical displacement relative to the horizontal displacement. The 2D vector map is generated by projecting the calculated displacements from the DIC onto a planar view, where each vector represents the direction and magnitude of movement at specific points, visualizing how the slope has shifted in x and y directions. To determine the 3D displacement, we first calculated the elevation changes across the DEMs as described above. This involved extracting elevation values from the "reference" DEM for each pixel and applying the DIC-derived x- and y-displacement values to adjust these coordinates. With the adjusted coordinates, we retrieved elevation values from the "after" DEM and computed the elevation differences for each pixel. Finally, to quantify the total displacement at each pixel, we calculated the Euclidean distance of the displacement vector by combining the x, y, and z displacements. This measure provides the total shift in position, reflecting how far each point has moved in 3D space. Additionally, we calculated the angle of vertical displacement relative to horizontal displacement by finding the arctangent of the vertical-to-horizontal displacement ratio. This angle indicates the tilt or steepness of the displacement, providing insight into the orientation and steepness of the movement relative to the horizontal plane.

To quantify the error threshold in our results, we evaluated the variability of displacement values within predefined stable zones. Displacement values were extracted from the total displacement raster within polygons representing the stable zones, and the average displacement for each polygon was calculated. The mean displacement within the stable zones, representing the potential threshold error, is 0.13 m for the period 2020–2022, and 0.08 m for the period 2022–2023.

3.4.3. Rock Fall Volume Calculation

To estimate the volume of a rock fall that occurred between the two SfM surveys conducted in 2022 and 2023, we employed the volume 2.5D tool of the CloudCompare software. First, we isolated the rock fall area by clipping the co-registered point clouds of the SfM surveys to focus on the region of interest. Using the Volume 2.5D tool, we then calculated the volume of the rock fall by comparing the pre- and post-event terrain elevation models, which allowed us to determine the amount of material removed by the rock fall.

3.5. Satellite Synthetic Aperture Radar

SAR imagery provides a valuable opportunity to observe slope movement over a significant time span, regardless of cloud cover or lighting conditions. InSAR is a technique that compares two SAR images acquired at different times, and generates an interferogram from them. These interferograms show phase differences across the area of interest, capturing a mix of factors such as orbital arrangements, terrain changes, atmospheric effects, and ground shifts (Bamler & Hartl, 1998). By carefully correcting topographic effects, atmospheric delays, and orbital errors, and using radar wavelength information, these phase differences can be converted into precise measurements of surface movements. InSAR has been widely used in slope movement analysis (e.g., Donati et al., 2023; Jacquemart & Tiampo, 2021; Manconi et al., 2024; Schaefer et al., 2024; Strozzi et al., 2018). From the processing step of generating interferograms, coherence images are a side product. The coherence images are important for quality-checking the InSAR data sets, as they indicate the level of correlation between the radar signals over time. High coherence values typically suggest stable, unchanged surfaces, while low coherence values may indicate areas with movement, surface changes, or poor radar signal reflection.

In this study, we used the Sentinel-1A and 1B radar satellites from the European Space Agency (ESA), operating at a 5.6 cm wavelength (C-band). We processed a total of 69 images from the ascending orbit and 63 from the descending orbit. Single Look Complex (SLC) images were acquired from the Alaska Satellite Facility (ASF) (downloaded from https://search.asf.alaska.edu, accessed on 18 December 2023). Our analysis of slope movement covers the period from 2015 to 2023 for the descending orbit, and from 2015 to 2021 for the ascending orbit, as only the descending orbit satellite remained operational after the end of 2021. Due to the presence of snow cover, we limited our data acquisition to the snow-free period from mid-June to the end of October. Interferograms were processed with temporal baselines of 12, 24, or 36 days.

To process the SAR data, we used the GAMMA software (Wegnüller et al., 2016). We applied a multilooking factor of 4 looks in range and 1 in azimuth to obtain square pixels and a final Ground Sampling Distance (GSD) of ~10 m. Topographic phase removal was performed using a 5 m resolution IfSAR DEM sourced from the Alaska Division of Geological and Geophysical Surveys (DGGS) platform (downloaded from https://elevation.alaska.

gov, accessed on 01 September 2023). Following co-registration and cropping of SAR pairs to our area of interest, we created differential interferograms and the corresponding coherence images. We then applied an adaptive filtering based on power spectrum analysis to mitigate phase noise and minimize residual artifacts. To address potential atmospheric phase delay effects, we applied an elevation dependent model (Strozzi et al., 2020; Wegnüller et al., 2016).

Our analysis includes the use of the generated coherence images and wrapped interferograms. Not all generated interferograms were usable due to decorrelation, which can arise from a number of factors such as snow cover, a significant time interval between two acquisitions, vegetation changes, high displacement rates of the landslide, and other environmental variables. Based on a selection criterion that considered radar coherence and visual inspection, we retained a total of 45 interferograms from the ascending orbit and 40 interferograms from the descending orbit.

3.5.1. Space-Borne DInSAR

Differential interferometric synthetic aperture radar (DInSAR) is used to detect surface displacement and is a widely used tool for mapping and analyzing landslides (e.g., Dini et al., 2019; Jones et al., 2021). To quantify slope displacements, we manually counted fringes in the ascending track interferograms using a reference point in a stable bedrock area. The total displacement d in the line of sight (LOS) direction was calculated using the formula: $d = (\lambda/2) \times N$, where λ is the wavelength of the radar signal and N is the number of fringes counted. We then converted the displacements to a velocity (in m/yr) by dividing the movement by the number of days between the interferograms and scaling accordingly. Manual fringe counting was repeated multiple times for accuracy, and the results were averaged to minimize human error. Interferograms were also processed with the descending orbit; however, due to the shadowing effect, it was not possible to clearly distinguish and count fringes. Additionally, when the LOS movement reaches and surpasses the radar's ability to accurately register phase changes (1.4 cm within one pixel relative to the next pixel), it can lead to potential phase aliasing (Manconi, 2021; Wasowski & Bovenga, 2014). For this study, we could identify a maximum of three fringes within a 12-day span, corresponding to a maximum measurable displacement rate of 2.56 m/yr.

3.5.2. Coherence Ratio

The coherence ratio method is helpful for detecting fast-moving landslides. While interferograms may struggle to capture rapid movements, the coherence ratio gives us insights into movement trends (until a certain limit), such as how the landslide can respond to heavy rainfall or temperature changes. Jacquemart and Tiampo (2021) demonstrated that it is possible to observe a decrease in the ratio right before a landslide collapse event. In this case, we used the ratio to understand the factors that influence movement over an extended and continuous snow-free period. To create a time series of the radar coherence ratio, we applied the same method as proposed in Jacquemart and Tiampo (2021). We calculated the average coherence in the area surrounding the two instabilities (see Figure 3a) and filtered out all coherence images with a mean coherence of less than 0.30. We established this mean coherence threshold as it represented the minimum value that allowed us to differentiate between the stable slope and the instabilities. After the selection process, we retained 38 coherence images for the ascending orbit and 33 for the descending orbit.

The coherence ratio (C_R) was determined by comparing the average coherence value of the unstable portion of the slope with the mean coherence of the surrounding stable slope (see Figure 3). We distinguished between Portage A and Portage B instabilities and computed the mean coherence for each area (Figure 3). Subsequently, we employed the same ratio calculation method as used by Jacquemart and Tiampo (2021), and as illustrated in the following formula:

$$C_{R1} = \frac{\gamma_{\text{Portage A}}}{\gamma_{\text{Stable Slope}}} \quad \& \quad C_{R2} = \frac{\gamma_{\text{Portage B}}}{\gamma_{\text{Stable Slope}}} \tag{1}$$

Given that our analysis was limited to the snow-free period, typically between late June and late October, we focused on the effects of temperature and precipitation within this time frame. This restriction meant that we could not fully assess seasonal impacts related to snowmelt or freeze-thaw cycles, instead concentrating on how temperature variations and precipitation during the summer and early autumn influenced landslide activity.

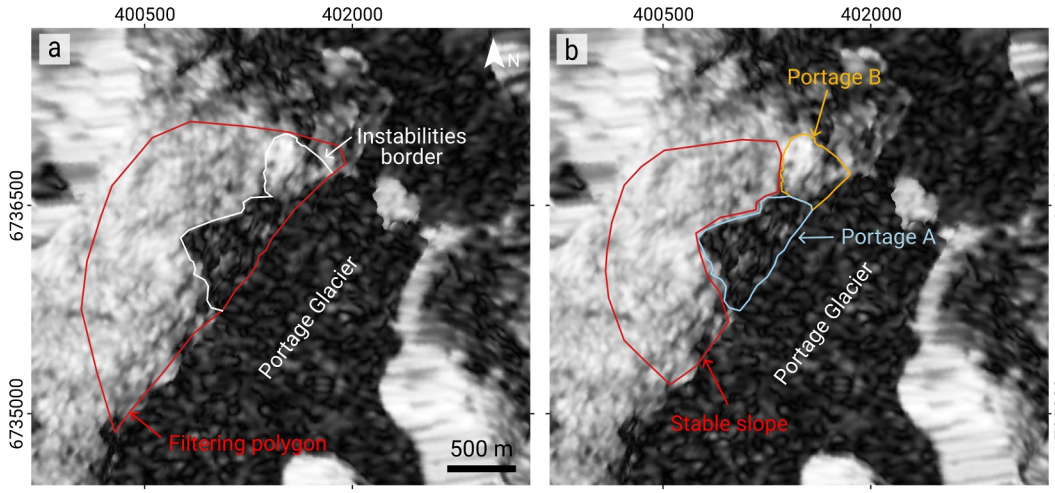

Figure 3. Interferometric coherence images of Portage slope and glacier. (a) Coherence image displaying the filtering polygon extent (red polygon) and indicating the border of the instabilities (white polygon). (b) Coherence image showing polygon extents for estimating the mean coherence of the stable slope (red polygon), Portage A (blue polygon), and Portage B (orange polygon).

3.6. Weather Data

Precipitation and air temperature data come from the National Oceanic and Atmospheric Administration (NOAA) platform. These data include daily cumulative precipitation, as well as minimum and maximum daily air temperatures. The weather station used for data collection is located at the Boggs Visitor Center, about 4 km away from the studied slope. The data were accessed from https://www.weather.gov/wrh/timeseries?site=PATO (accessed on 10 April 2024) and were used without further processing.

We used ERA5-Land data to fill data gaps in the time series from the weather station. We extracted precipitation and temperature values from ERA5-Land (Muñoz-Sabater et al., 2021) and calculated the daily average from the four pixels surrounding the landslide center point. Over the reference period 2010–2020, we computed correction factors as follows:

$$T_{\text{corr}} = T_{\text{avg,stat}} - T_{\text{avg,ERA5}} \tag{2}$$

$$P_{\text{corr}} = P_{\text{tot,stat}}/P_{\text{tot,ERA5}} \tag{3}$$

where $T_{\text{avg,stat}}$ and $T_{\text{avg,ERA5}}$ are the average temperatures from the station and the ERA5 data, respectively, over the reference period, and $P_{\text{tot,stat}}$ and $P_{\text{tot,ERA5}}$ are the total precipitation from the station and ERA5 data, respectively, over the reference period. The debiased time series could then be calculated

$$T_{\text{debias}} = T_{\text{ERA5}} + T_{\text{corr}} \tag{4}$$

$$P_{\text{debias}} = P_{\text{ERA5}} * P_{\text{corr}} \tag{5}$$

where T_{ERA5} and P_{ERA5} are the raw ERA5 time series over the pixels of interest, $T_{\text{corr}} = 3.5°\text{C}$, and $P_{\text{corr}} = 0.88$. To construct a final time series, we used station data on days when it was available, and the debiased ERA5 time series to fill the gaps (86 and 83 days for precipitation and temperature, respectively).

4. Results and Interpretation

4.1. Progressive Spatial Evolution and Morphological Characteristics of the Instabilities

The unstable slope above the Portage Glacier is composed of two distinct segments, referred to as "Portage A" and "Portage B" (also see Schaefer et al., 2024), that progressively developed spatially in the up-glacier direction (Figure 4). Portage B, near the glacier terminus, was the first segment of the slope to become unstable, followed

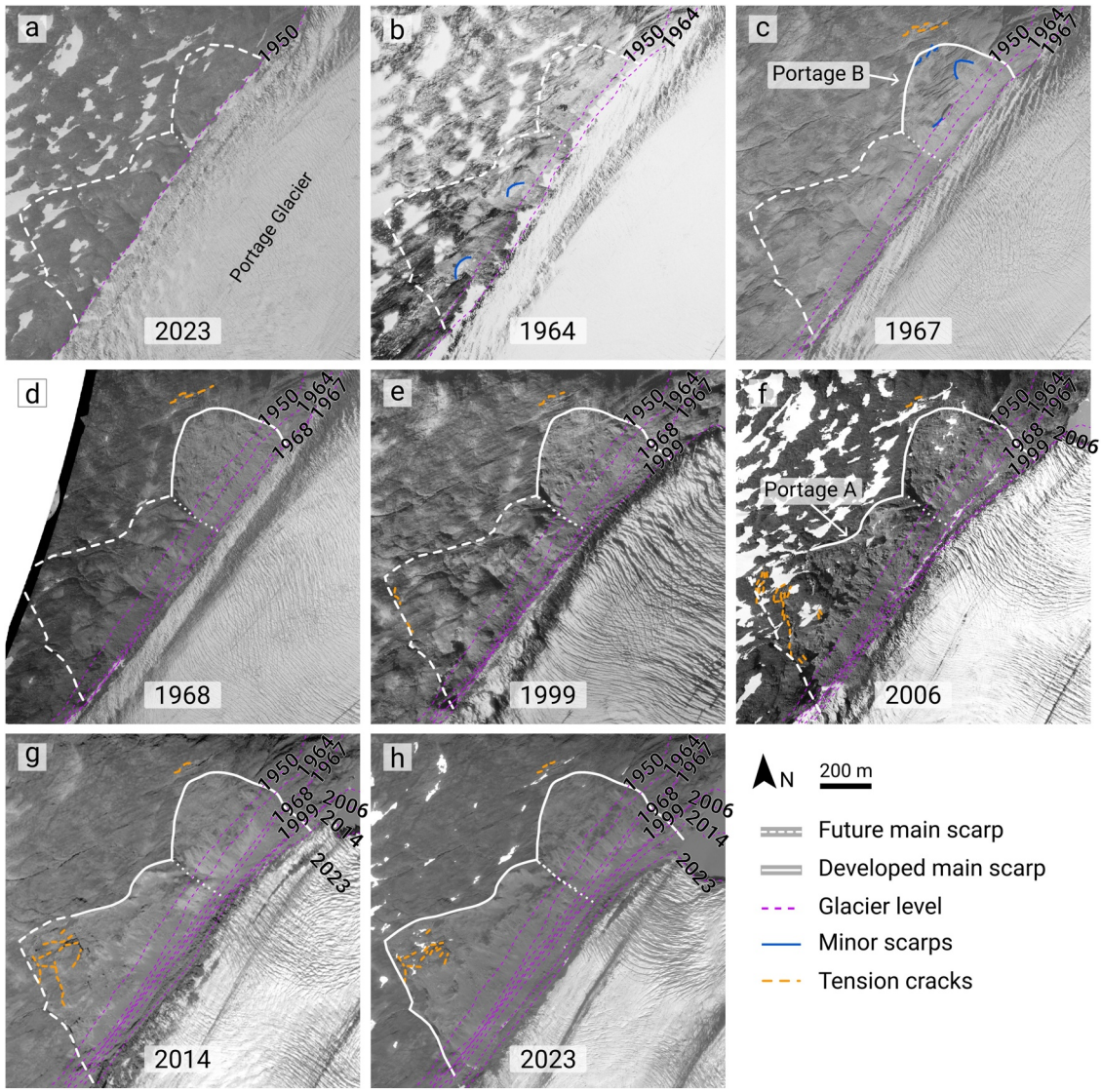

Figure 4. Temporal and spatial evolution of Portage A and Portage B instabilities based on interpretation of aerial images from (a) 1950 (USGS); (b) 1964 (USGS); (c) 1967 (USGS); (d) 1968 (USGS); (e) 1999 (USGS); (f) 2006 (USGS); (g) 2014 (ESRI Wayback imagery); (h) 2023 (ESRI Wayback imagery). The dotted line indicates the boundary between Portage A and Portage B.

~32 years later by Portage A (Figure 4). In 1950, the slope appeared intact, with no sign of deep-seated deformation (Figure 4a). In 1964, five months after the devastating Great Alaskan earthquake (Mw = 9.2), the slope showed some minor collapses/rock falls (see blue lines in Figure 4b). The first clear signs of deep-seated deformation were visible for Portage B in 1967, with the development of parts of the main scarp, tension cracks and rock falls (see orange lines on Figure 4c). By 1968, Portage B reached its current extent, with minimal observable changes since then (Figure 4d). Portage A, on the other hand, exhibited no clear indications of deep-seated deformation until 1999, although rock fall talus accumulation at its toe was observed. In 1999, tension cracks became visible at the up-glacier margin of Portage A, coinciding with the location of the most recent main scarp (Figure 4e). By 2006, Portage A had extended about 480 m up-glacier, with its main scarp becoming prominently visible, particularly in the upper section. The remaining ~300 m of the slope, corresponding to its current extent, is characterized by numerous tension cracks (Figure 4f). Optical satellite imagery shows that between 2014 and 2016, Portage A progressively expanded up-glacier to its current extent (Figure 4h).

Both instabilities exhibit distinct morphological characteristics, in line with their different stages of spatial and temporal evolution (Figure 4). The Portage slope shows significant bedrock fracturing and the unstable areas are

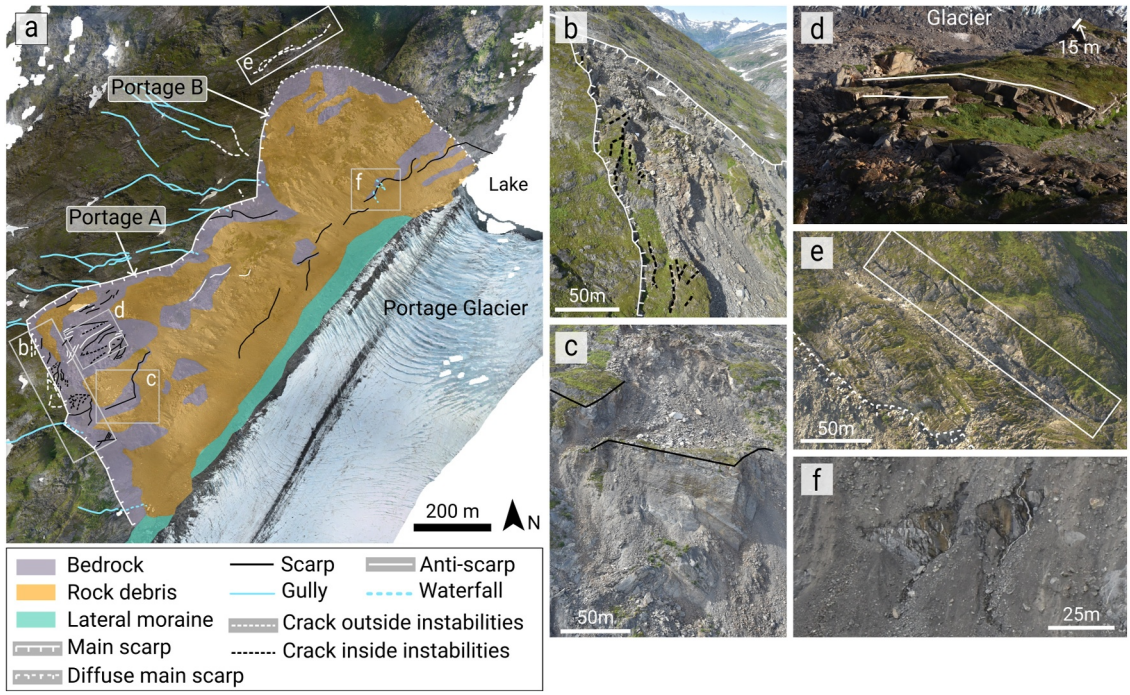

Figure 5. Geomorphological overview of the slope at Portage Glacier. (a) Hillshade map from the 2023 SfM DEM highlighting geomorphological key features (b) photo of the detachment zone within Portage A (viewed from SW toward N), (c) photo of a significant bedrock block situated in Portage A (viewed from SE toward NW), (d) photo of anti-scarps located in Portage A; arrow shows 15 m scale (viewed from NW toward SE), (e) photo of a prominent crack above Portage B (viewed from SW toward N), (f) picture on the emergence of springs within Portage B (viewed from SE toward NW).

characterized by deep-seated deformation structures such as scarps (downhill-facing scarp), anti-scarps (uphill-facing scarp), tension cracks, tilted blocks, and rock debris stemming from local rock falls (Figure 5). Portage A is characterized by a well-defined main scarp that clearly delineates the unstable zone. Large portions of exposed bedrock protrude from the slope and are interspersed with debris from previous deformation and rock falls (e.g., Figure 5c). Along the up-glacier boundary of Portage A, numerous bedrock blocks topple and detach from the margin of the instability (Figure 5b). Several distinct scarps and anti-scarps are visible in the bedrock within the unstable slope (Figures 5a and 5d). These features are mainly concentrated in the most active part of Portage A and illustrate the current internal movement. In contrast, the Portage B instability border is not associated with such a clear scarp. The outer boundary is in some parts not delineated by a distinct vertical scarp, but instead consists of a series of fragmented bedrock blocks (Figure 5a). Portage B does not feature large blocks of exposed bedrock, as observed at Portage A. Numerous tension cracks extend across the slope near the delineated margins of the instability, some with clearly defined traces stretching over 150 m (e.g., Figure 5e). The slope toes of both instabilities comprise a mixture of rockfall debris and lateral moraine material, with ongoing deposition complicating precise boundary delineation (Figure 5a).

Rock fall is a common process across both instabilities, contributing to ongoing slope degradation and leading to the accumulation of talus at the base. Between 2022 and 2024, four major rock falls were observed (Figure 6a). At the toe of Portage B, a progressive collapse (red outline in Figure 6b) was observed starting on 10 October 2022. Time-lapse images captured by a camera installed on the opposite side of the valley in summer 2022 reveal that the collapse initiated in the lower portion of the mass and gradually progressed upward over subsequent weeks, with the most drastic changes occurring between 10 and 17 October. In 2020, the failure area was still partially covered by the glacier. By October 2022, the glacier had retreated to the up-glacier edge of the 2022 local collapse zone (Figure 6b, red polygon). The estimated rock volume (see Section 3.4.3) of this collapse is approximately 115,000 m^3. In November 2022, another rock fall (blue outline in Figure 6a), occurring at the up-glacier margin of Portage A, was identified in the time-lapse camera images. This source area has been the site of several rock falls. In mid-April 2023, another rock fall from the up-glacier margin of Portage A was observed on PlanetScope

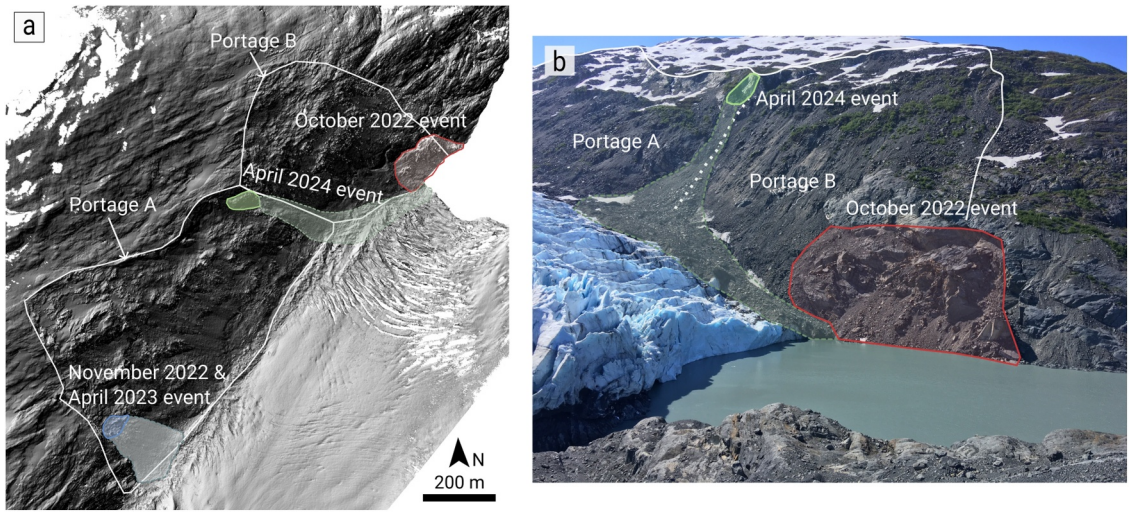

Figure 6. Recent major rock fall activity. (a) Location of the rock falls and their run-out extent, with red polygons indicating the rock fall that occurred in October 2022, blue polygons showing the rock fall that occurred in November 2022 and April 2023, and the green polygon representing the rock fall in April 2024. (b) Photo of the October 2022 and April 2024 rock falls (photo from 17 June 2024, credit: Ian Moore). The white dotted line indicates the boundary between Portage A and Portage B.

imagery. The event had a runout distance of more than 200 m. A third collapse occurred at the border between Portage A and B between 24 and 26 April 2024 (green outline in Figure 6a).

Additionally, the presence and behavior of several gullies, water sources and waterfalls around and within the instabilities reveal intricate and dynamic hydrological processes. In some cases, surface water flows from stable ground outside the instability over waterfalls into the unstable area before rapidly infiltrating into the unstable part of the slope. In other cases, surface streams disappear into cracks or seep into the subsurface at the outer margin of the instabilities. Intermittent springs or localized water flows occasionally appear within the unstable slope area (e.g., Figure 6f). These phenomena suggest complex subsurface water pathways that intercept and redirect water within the moving rock mass of the slope. The pictures from the time lapse camera reveal a potential correlation between precipitation events and the behavior of some of these waterfalls, with changes in water flow being observed almost immediately following heavy rainfall (see Figure S2 in Supporting Information S1).

4.2. Glacier Evolution During Slope Deformation

The temporal and spatial changes of Portage Glacier at the locations of Portage A and Portage B provide important context for understanding the timing of the slope deformation. Figure 7a illustrates the changes in Portage Glacier from 1950 to 2023 at the locations of Portage A and Portage B. In 1950, the glacier elevation was up to 300 m higher than that in 2023. The white arrows in Figure 7a provide an approximate extent of the glacier during the period when clear signs of a deep-seated rock slope instability became visible in the historical imagery (cf. Section 4.1). Between 1964 and 1967, marking the initiation of deep-seated movement of Portage B, the glacier height at the toe of Portage B decreased significantly. In contrast, at the site of Portage A, the height decreased by only about 10 m during these years. During the development of Portage A, between 1999 and 2006, the glacier experienced a reduction in height of approximately 30 m (Figure 7e). Both instabilities were activated when the glacier reached a similar elevation range, with Portage B initiating when the glacier was between 180 and 200 m a.s.l., and Portage A initiating when the glacier was between 200 and 220 m a.s.l.

4.3. Structural Setting

The Portage area is characterized by a complex geology including folding structures (on a meter-scale) and closely spaced joints and bedding that occur across the entire slope. Based on field mapping and measurements of the SfM point clouds, we identified five distinct discontinuity sets labeled as J1 through J5 (Figure 8). Among these sets, J1, J3, J4, and J5 strike in an NNE-SSW direction, with J1 and J4 being sub-vertical, while J3 and J5 dip at about 35° SE and 20° NE, respectively (Figure 8a). The J4 set corresponds to the bedding (Figures 8d and 8e) and J3 is sup-parallel to the slope orientation (Figures 8a and 8d). J2, on the other hand, exhibits a sub-vertical dip

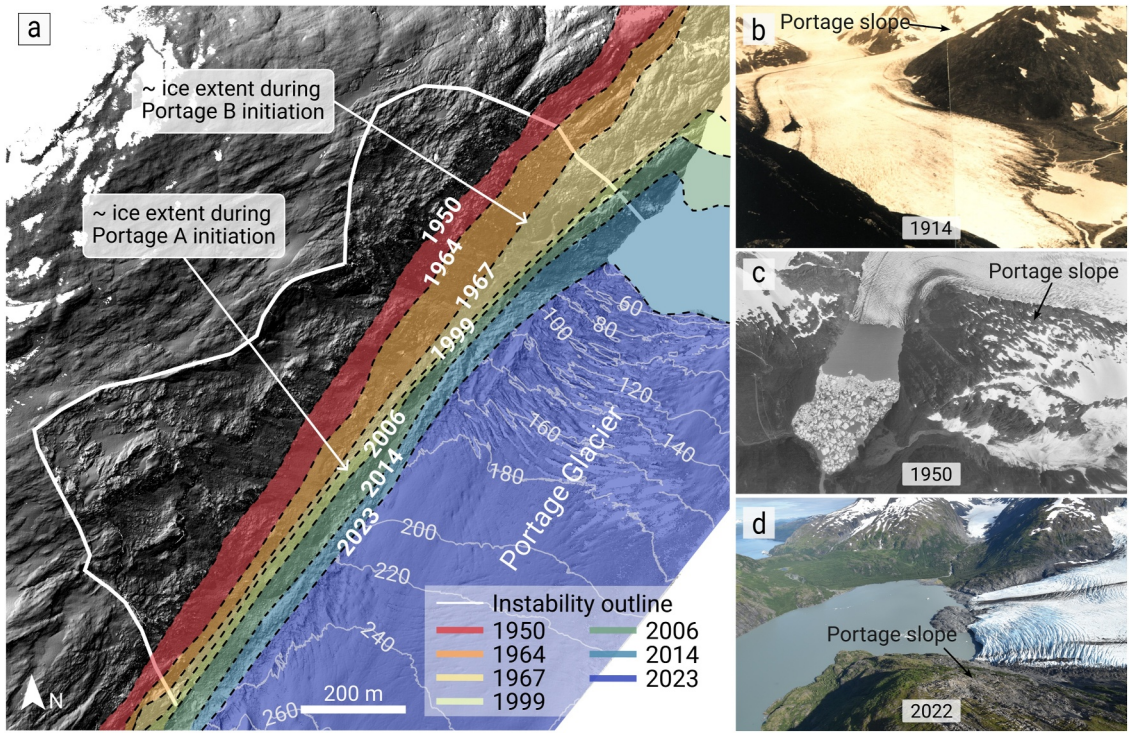

Figure 7. Historical overview of the evolution of Portage Glacier (a) Illustrative map showing the progressive retreat of Portage Glacier from 1950 to 2023. The background map is a hillshade derived from the 2023 SfM DEM (b) Photography of Portage Glacier toward SE in 1914 (NOAA Digital collections) (c) Photography of Portage Glacier from the top in 1950 (USGS) (d) Photography of Portage Glacier from the top of the slope in 2022.

with a WNW-ESE strike (Figure 8c). Along the up-glacier border of Portage A, J2 aligns with the lateral scarp of the unstable slope (Figure 8b). The west part of the Portage B main scarp follows the orientation of the J1 joints set (Figure 8b). The orientation of discontinuity set J4 (i.e., bedding) is aligned with the upper part of the scarp of Portage A and Portage B (Figure 8b). About 600 m up-glacier from the boundary of the unstable, a hinge zone of a large fold is visible (Figure 8f).

4.4. Slope Displacements

To quantify the slope displacements from July 2015 to April 2024, we combined data from LiDAR, photogrammetry, and InSAR. Here, we present a temporal analysis of slope movement for both instabilities, Portage A and Portage B, organized as follows: (a) general observations of annual slope movement patterns and (b) characterization of short-term displacement trends of the slope.

4.4.1. (Multi-)Annual Slope Displacement Characteristics

Elevation change analyses over the periods of 2015–2020, 2020–2022, and 2022–2023 are shown in Figure 9. During all three time periods, Portage A shows an alternating pattern of surface lowering and uplift, characterized by features (e.g., Figure 5b) indicative of a toppling mechanism, with elevation loss in both the upper and lower sections, while the middle section exhibits only a slight elevation gain. This sequence differs from the typical slump-bulge pattern characterized by a slump-area at the headscarp and bulging area at the toe. The observed elevation change patterns suggest that the Portage slope does not behave as a single coherent block but rather shows internal deformation indicative of a structurally segmented landslide material. In the bedrock on the southwestern edge of Portage A, we observe both negative and positive elevation changes. This pattern results from deformation processes, including translational sliding (described below), as well as internal rockfall and deposition. Within this area, we identified scarps and anti-scarps aligned with the orientation of bedding J4 (Figure 5a).

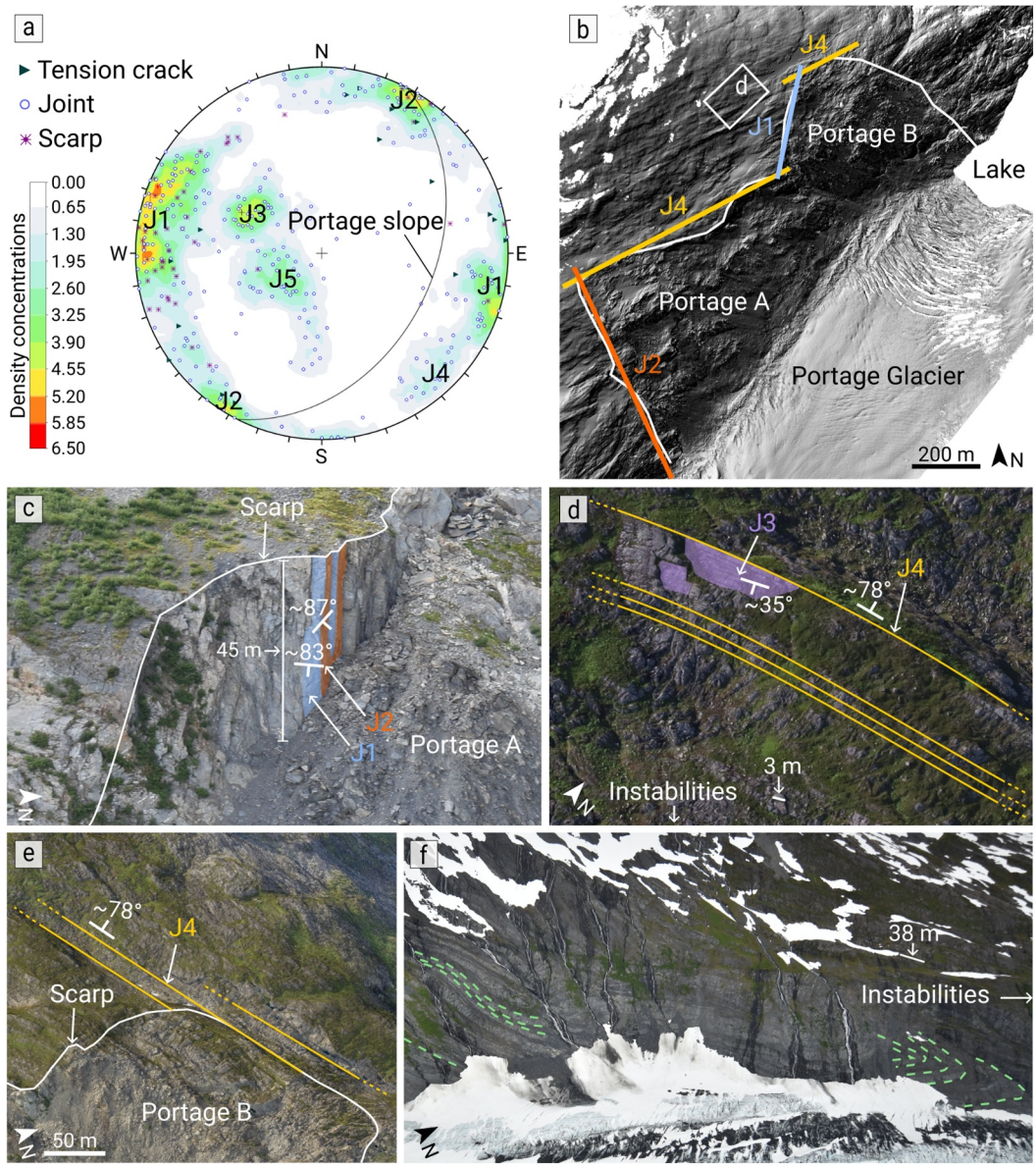

Figure 8. Structural analysis of the mapped discontinuities at the Portage slope. (a) Stereonet displaying poles and pole density with the great circle representing the slope orientation. (b) Hillshade map showing the discontinuities J1, J2, and J4 along the scarp (white line). The colored lines are schematic representations of the joint sets determining the scarps. (c) Photograph of the left scarp border of Portage A showing discontinuities J1 (blue polygons) and J2 (orange polygons). (d) Photograph of an outcrop outside of the unstable area showing the discontinuities J3 (purple polygon) and J4 (yellow lines). (e) Capture of the SfM point cloud of the top of Portage B instability showing the bedding J4 (yellow lines). (f) Photograph of the slope about 600 m further up-glacier with the dashed lines showing changes in the geological structures, including fold hinges and orientations of folded layers.

Portage B, in contrast, displays little elevation change across most of the unstable area, with changes at or below the DEM differencing error threshold of 0.4 m. The base of the slope, however, experienced significant elevation loss up to 4 m, particularly between 2022 and 2023 associated with the rockfall event in 2022 (Figure 6). Between 2020 and 2022 (Figure 9c), most of the significant changes (>1 m) within the top and central part of the slope at Portage B are due to vegetation changes.

At the toe of the slope, a surface lowering of up to 9 m is observed in the talus. The lower ∼80 m of the talus slope, composed of a combination of rock debris and the lateral moraine, subsided by over ∼5–9 m (±1.9 m) between 2015 and 2020, by 2–6 m (±0.36 m) between 2020 and 2022, and ∼1–3 m (±0.43 m) between 2022 and 2023

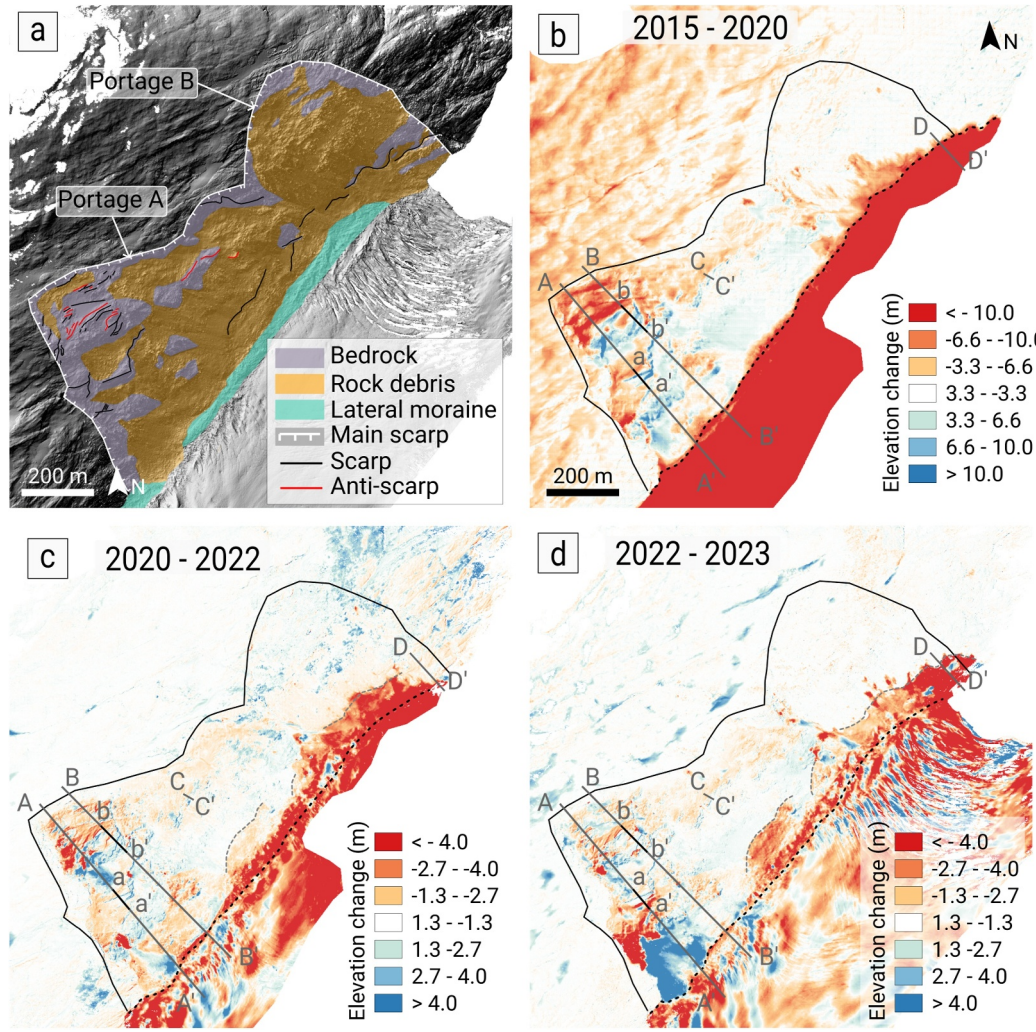

Figure 9. (a) Geomorphological map (b) cumulative surface elevation change maps using DEM differencing over a 5-year span (differences between IfSAR 2015 (DGGS) and LiDAR 2020 (DGGS)), (c) over two years (differences between LiDAR 2020 (DGGS) and SfM DEM 2022), (d) over one year (differences between SfM DEM 2022 and SfM DEM 2023). Black outlines represent the mapped instability boundaries. Dark gray lines indicate the location of profiles shown in Figure 10. The black dashed lines mark the approximate boundary between rock debris material and glacier ice. Gray dashed lines highlight newly formed scarps in the lower parts of the slope.

(Figure 9). The Movie S1 in the supporting information illustrates the formation of scarps and movement in the lower parts of both unstable zones, corresponding to the areas marked by gray dashed lines in Figures 9c and 9d.

Outside the instability boundaries, significant elevation variations mostly on the upper part of the slope are observed, likely related to changing snow conditions between the different DEMs. Despite this potential source of noise, the elevation change analysis conducted over the specified periods reveals meaningful patterns of slope movement within the Portage A and B instabilities (Figure 9).

The cross sections of Portage A (Figure 10 and Figure S3 in Supporting Information S1) show movement across the upper section of the slope. The profiles show that the elevation change component is not the only component of the movement, but rather a combination of vertical and horizontal movement. Overall, we observe a vertical displacement up to ~5–7 m (±1.9 m) between 2015 and 2020, ~2–2.5 m (±0.36 m) between 2020 and 2022, and ~1.5–2 m (±0.43 m) between 2022 and 2023. The displacement of these features down and across the slope suggests a translational sliding behavior.

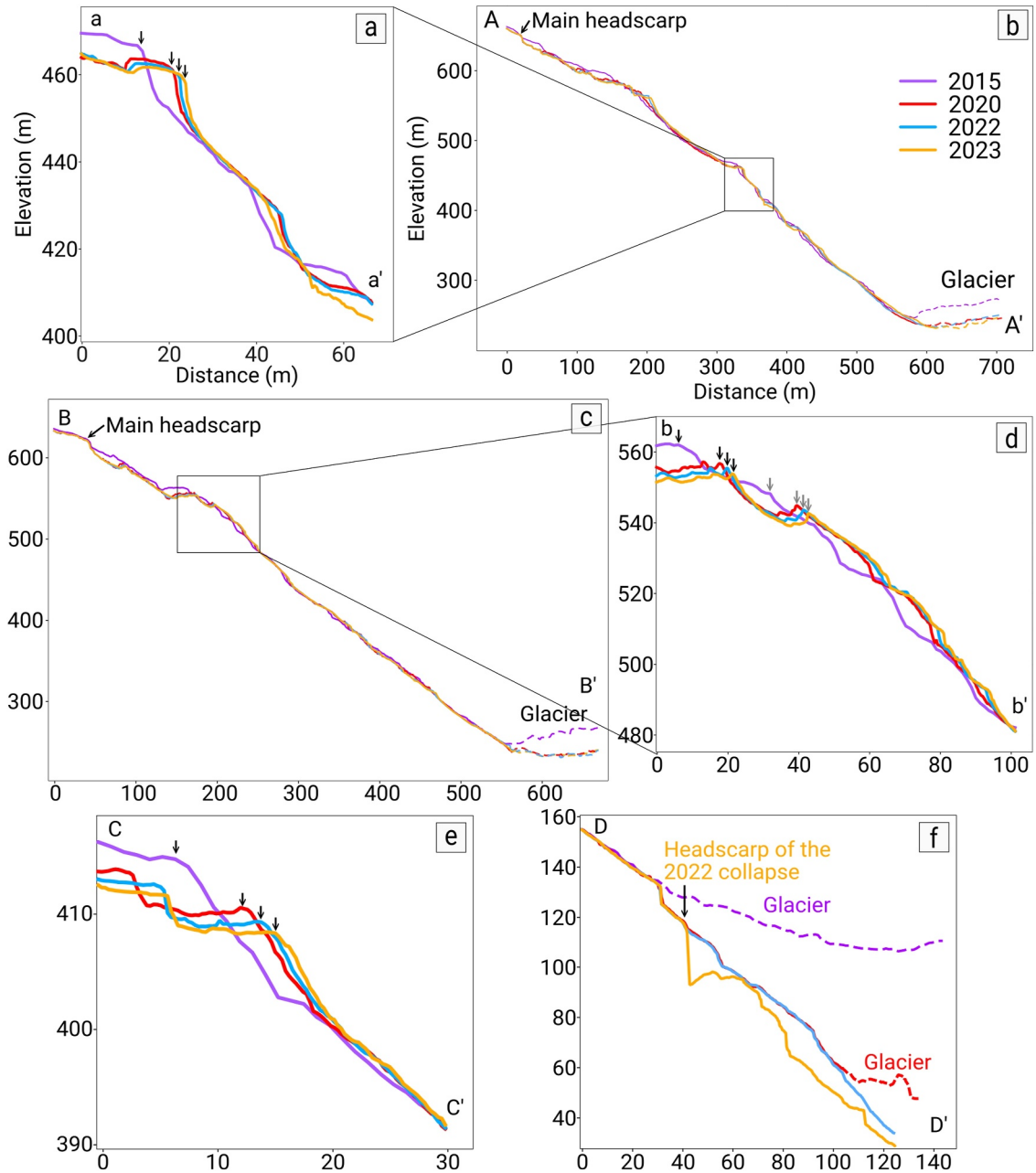

Figure 10. Elevation change between 2015, 2020, 2022, and 2023 across profiles. (a) Profile a-a', (b) Profile A-A′, (c) Profile B-B′, (d) Profile b-b', (e) Profile C-C′, (f) Profile D-D'. The black arrows highlight changes over time for distinct features such as blocks or scarps. The localization of the profiles is shown in Figure 9.

The findings of the feature tracking over the periods of 2020–2022 and 2022–2023 are illustrated in Figure 11. Overall, we observed similarities in the direction of displacements between 2020 and 2022 (Figure 11a) and between 2022 and 2023 (Figure 11b). The displacement vectors found in Portage A suggest a dominant displacement normal to the glacier axis with a smaller down-glacier component (Figures 11a and 11b). We observe a change in direction from the top to the bottom of Portage A: in the upper part, the *x*-component of the movement is slightly directed toward the lake, while the central and bottom parts of the slope exhibit movements perpendicular to the glacier (in *y*- direction). In turn, the dip angle of the displacement vectors (Figures 11e and 11f) shows that the ratio of horizontal displacements to vertical displacements generally increases from the top to the bottom of the instabilities. Cumulative total 3D displacement is shown as a heat map in Figures 11c and 11d. The total displacements are concentrated in the same areas as the observed elevation changes (Figures 9b and 9c).

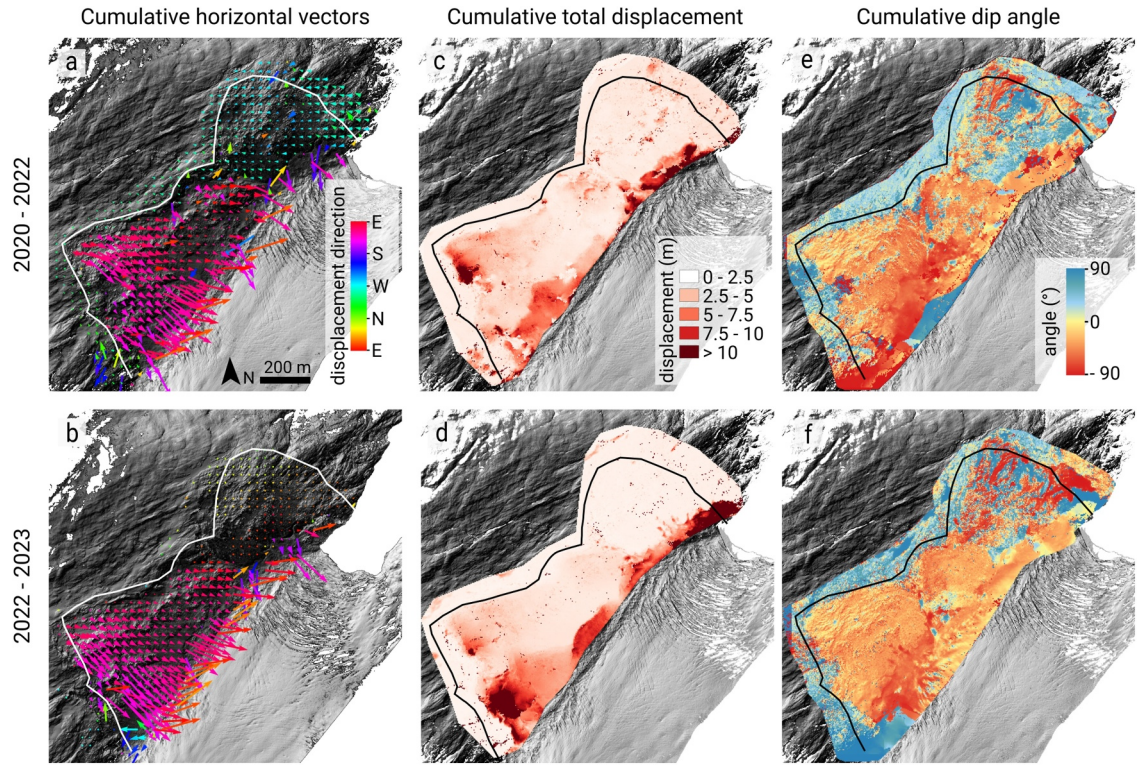

Figure 11. Cumulative horizontal and vertical displacement between 2020–2022 and 2022–2023 using DIC and elevation changes. (a) and (b) The 2D displacement, which combines both horizontal *x*- and *y*- displacements, is shown as exaggerated vectors and color-coded by movement direction (north, south, east, west) to further illustrate the movement patterns for the periods 2020–2022 and 2022–2023, respectively. (c) and (d) Total displacement (combined *x*, *y*, *z* components) shown as a heat map for the periods 2020–2022 and 2022–2023, respectively. (e) and (f) Dip angle of the movement between 2020–2022 and 2022–2023, respectively.

The up-glacier edge of Portage A emerges as one of the areas most affected by deformation, similar to the results of the elevation change analysis. The toe of the slope, composed of rapidly changing talus, underwent the most significant change during both time spans (2020–2022 and 2022–2023). These talus deformations are likely influenced by glacier movement, which can displace and disturb the talus material. Notably, some of the surface lowering in the lower part of the slope, such as the scarp opening visible in Figures 9b and 9c (and Movie S1), can be attributed to the direct influence of the short-term glacier surface lowering. The effect of the glacier movement and thinning on the talus deformation is also visible in Figure 11b, where the lower central part of the slope shows clear downward movement due to the glacier surface lowering, as well as a glacier-parallel component due to deformation caused by the glacier motion.

4.4.2. Short-Term Slope Displacement Characteristics

The interferograms analyzed during the study period (July 2015–September 2021) reveal three primary domains affected by displacements (see Figure 12a): two within the Portage A segment (D1 and D2) and one within Portage B (D3). In D1 and D2, the patterns of fringes change over time (see Figure 12, Figure S4–S6 in Supporting Information S1). D1 exhibits large displacement rates causing decorrelation in the interferograms (e.g., Figure 12c). The displacement data obtained from the interferograms for D2 show that LOS displacement rates vary widely, ranging from 0.14 m/yr to the upper limit of distinguishable fringes (>2.56 m/yr). These rates, measured over roughly the same time period, are up to about two orders of magnitude faster than those reported by Schaefer et al., 2024. Portage B displays very few fringes, usually less than ¼ of a fringe, making it sometimes challenging to interpret the magnitude and orientation of the movement on the LOS. The LOS movement of D3 varies from 0 to 0.28 m/year.

Portage A exhibits variations in movement rates and directions between the domains D1 and D2. Over time, these two domains sometimes move together in sync but can also differ in both movement rate and direction (Figure 12, Figure S4–S6 in Supporting Information S1). Between 2015 and 2018, the two compartments D1 and D2 of

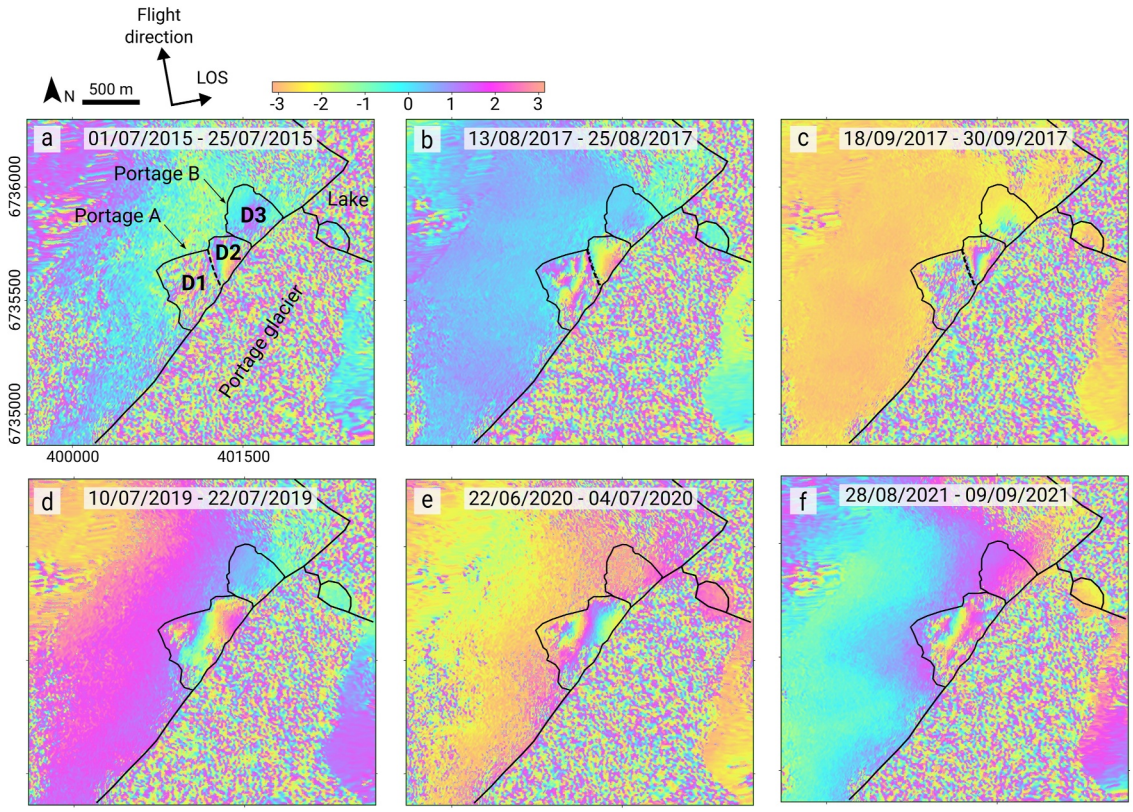

Figure 12. Evolution of Portage slope movement between 2015 and 2021 using DInSAR (from the ascending orbit). (a–f) display interferograms between respective dates. The black lines delineate the two instabilities, Portage A and Portage B, and the black dashed line indicates the three domains (D1, D2, D3) within these instabilities.

Portage A typically show differences in displacement rates, with larger displacement rates in D1. However, from 2019, the movement of D1 and D2 generally aligns (e.g., Figures S5d–S5f in Supporting Information S1), with both domains generally exhibiting similar displacement rates, although some exceptions remain (e.g., Figure S5j in Supporting Information S1). Similar to the displacement rates, the displacement directions of D1 and D2 change over time. During periods of similar rates, the movement direction of D1 and D2 shows parallel movement direction, which is perpendicular to the glacier. For periods when D1 moves more rapidly than D2, the D1 overall displacement direction exhibits a component toward the lake, despite D2 remaining perpendicular to the glacier.

Additionally, we analyzed slope movement by exploiting the coherence ratio from both ascending and descending orbits between July 2015 and October 2023. The analysis focused on Portage A and Portage B, rather than the subdomains D1 to D3. The time series of the coherence ratio (Figure 13) for Portage A shows a decreasing trend throughout the summer months. From early July to late October, the coherence ratio decreased, indicating that the instability became increasingly decorrelated and suggesting an increase in activity. This trend is particularly evident in the years 2017–2020, and 2023 (Figure 13). Portage B, on the other hand, maintains a higher coherence ratio, consistent with the previous analyses.

We also investigated the relationship between the coherence ratio and meteorological data. No significant response in the coherence ratio was detected due to temperature changes, which generally remained above 5°C throughout the summer and gradually declined in early autumn. Some precipitation events were associated with a decrease in the coherence ratio for Portage A. Notably, in 2017, it appears that intense and prolonged rainfall caused a significant decrease in the coherence ratio. However, no such correlation was observed for Portage B. This suggests the differing sensitivity of the two instability bodies to precipitation events.

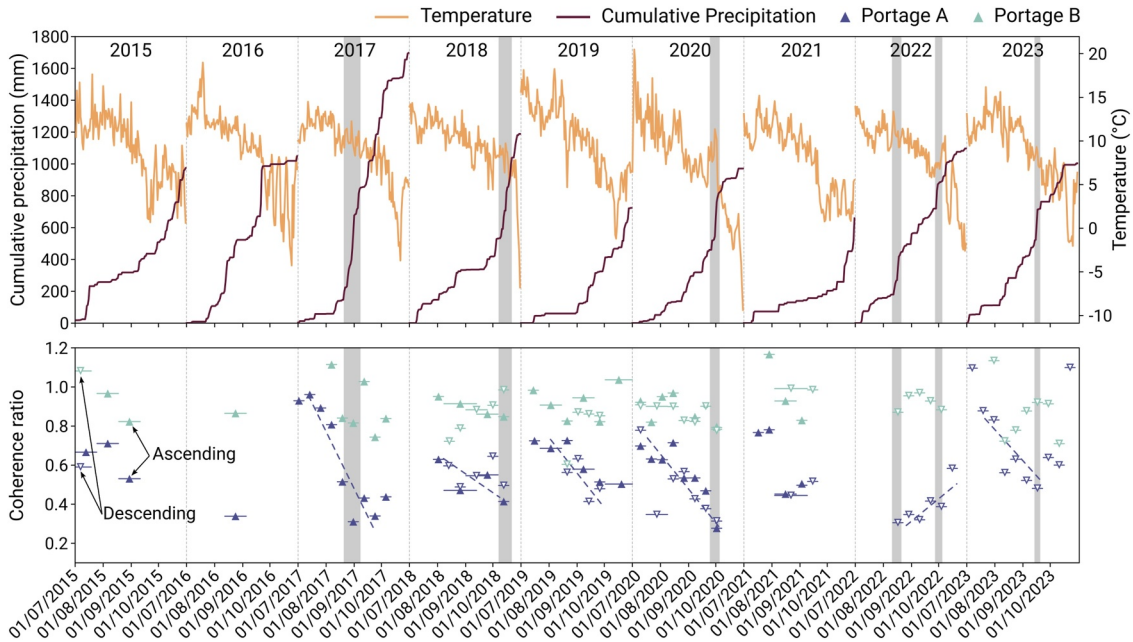

Figure 13. (Upper plot) Cumulative precipitation and air temperature from 2015 to 2023, with data limited to July, August, September, and October. (Lower plot) Radar coherence ratio for both ascending and descending orbits, for Portage A and Portage B instabilities, during the same period. The horizontal lines behind each symbol indicate the temporal baseline (12-day, 24-day, or 36-day) and the colored dashed lines show the trend of the data plotted. Heavy precipitation events are highlighted by the gray rectangles.

5. Discussion

5.1. Structural Control and Slope Kinematics of Paraglacial Rock Slopes

The mechanical behavior of rock masses in alpine environments is fundamentally governed by their structural features, including the presence and orientation of discontinuity sets, folds, and faults (Stead & Wolter, 2015). Structural preconditioning, wherein pre-existing discontinuities govern the mechanical response of slopes, has been widely recognized as a key factor in controlling rock slope instability, particularly under changing environmental stress regimes (e.g., Agliardi et al., 2013; Lemaire et al., 2020; Vick et al., 2020). In paraglacial settings, such structurally controlled failures have been widely documented (e.g., Agliardi et al., 2013; Augustinus, 1995; Bovis, 1982; Donati et al., 2023; Glueer et al., 2020; Klimeš et al., 2021; Kos et al., 2016; Lemaire et al., 2024; McSaveney, 2002; Rechberger et al., 2021).

This case study at Portage Glacier contributes to the growing body of evidence emphasizing that structural preconditioning is a key factor in controlling paraglacial rock slope failures. The geology of the site, dominated by greywacke, features prominent bedding planes and discontinuity sets that control instability boundaries and failure mechanisms (Figure 14). Since the main sliding surface does not yet daylight, the depth of the instabilities is likely to exceed 15 m. Additionally, the results from the interferogram analysis show that Portage A is divided into two domains, D1 and D2, that can move independently. The shape of the fringes at the boundary of this differential movement aligns with the orientation of discontinuity J2, which also serves as the current up-glacier boundary of Portage A (Figure 14c). The kinematic analysis of the geological structures suggests a translational sliding mechanism along the ~35° inclined dip-slope structures (J3) (Figure 14). Furthermore, toppling is primarily possible along J1 and J4 discontinuities, which both show a large persistence and are found ubiquitously (Figure 14). The latter corroborates the observation of large toppled bedrock sections within the unstable area (Figure 5b), the orientation of the northern scarps, and up-hill facing scarps (Figure 5). The mapped discontinuities are well-suited to promote toppling, sliding, or a combination of both, which can result in local failures (e.g., Figure 6).

The results of the elevation change analysis (Figure 9) further support the interpretation that translational sliding and toppling are the primary failure mechanisms (ref. to Hungr et al. (2014) classification). This is particularly evident in the bedrock section of Portage A, where a sequence of alternating negative and positive surface changes

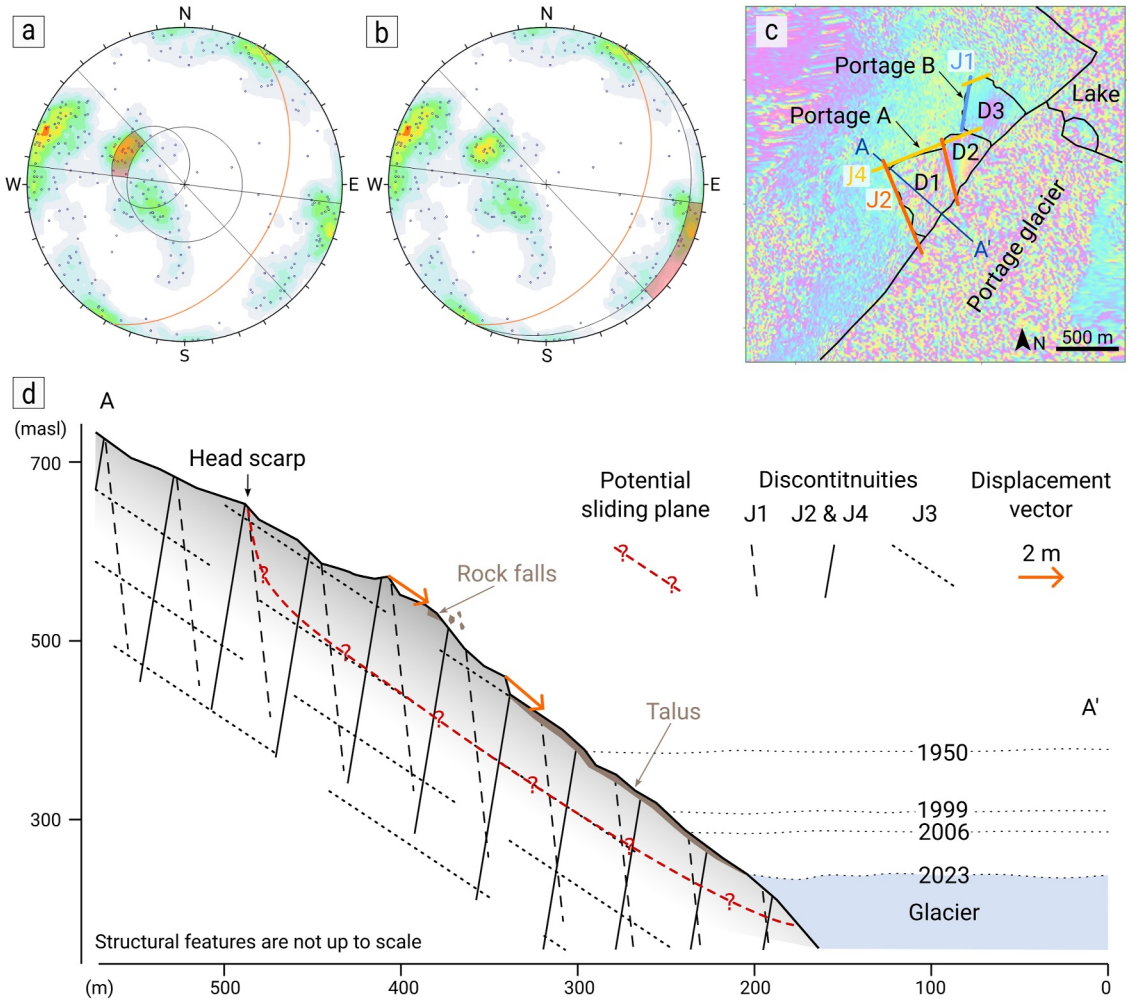

Figure 14. Rock slope kinematic analysis for (a) planar failure mode and (b) flexural toppling. (c) Interferogram (01/07/215–25/07/2015) and (d) Structural profile illustrating the main discontinuities (discontinuity spacing not to scale) and glacier height levels over time for reference.

is observed (Figure 9). The slope kinematic is also corroborated by observations in the profiles of Figure 10, where areas of relatively flat topography are associated with negative surface changes, whereas steep terrain is characterized by prominent anti-scarps and positive surface changes.

These results underscore the dominant role of structural geology in conditioning the spatial evolution of the rock slope in a paraglacial setting. This aligns with the findings of Augustinus (1995), who emphasized the influence of rock type and structural conditions in shaping paraglacial slope response to glacier erosion and debuttressing. In particular, that study demonstrates that schist and greywacke slopes in the Southern Alps of New Zealand, due to their closely spaced joints and foliation, are particularly prone to large deformation and failure after deglaciation, in contrast to massive plutonic rocks, which tend to respond through more superficial processes such as rock fall.

5.2. Role of Glacier Thinning in Structurally Preconditioned Rock Slopes

Some landslides in paraglacial environments may undergo catastrophic failure regardless of whether the glacier has fully retreated or not (e.g., Higman et al., 2018; Lemaire et al., 2024; McColl et al., 2010), while many slopes, despite experiencing glacier retreat and thinning, remain stable and do not fail. This variability reflects the complex ways in which rock slopes respond and adjust to glacial changes. In paraglacial environments, slope adjustment to glacier change can manifest in several ways: (a) sudden catastrophic failure; (b) large deformation, characterized by slow progressive movements, that may eventually result in catastrophic failure; and (c) frequent rock falls, representing rapid adjustment of steep rock faces and typically resulting in talus accumulation at the

slope toe (Ballantyne, 2002). At Portage Glacier, these processes are clearly expressed: widespread talus and rock fall deposits (Figures 5 and 6) highlight the short-term slope response, while the ongoing deep-seated deformation (Figures 9 and 12) reflects the long-term slope adjustments to the continuously evolving conditions at the slope toe. These earth surface processes exemplify the dynamic geomorphic adjustment of steep bedrock slopes in response to glacier changes, similar to observations from slopes in other (formerly) glaciated regions worldwide, including the European Alps (e.g., Kos et al., 2016; Rechberger et al., 2021), New Zealand Southern Alps (e.g., Cody et al., 2020; McColl and Davies, 2013; McSaveney, 2002), Andes (e.g., Klimeš et al., 2021; Sepúlveda et al., 2023), and the Southeastern Tibet Plateau (e.g., Zhong et al., 2021).

At Portage, the structural discontinuities and bedding planes predispose the slope to failure, but the observed movement patterns cannot be explained without considering the role of glacier thinning. The three domains (D1, D2, and D3) can move independently from each other even though they share similar lithology, structural geology, and are influenced by the same precipitation and seismic conditions. The only changing boundary condition among the domains over time is the glacier level. The thinning of the glacier was not homogenous at Portage B and Portage A, with the glacier thinning relative to the slope at Portage B being more pronounced than at Portage A (Figure 7a). However, despite these differences, our results show that both Portage A and Portage B started to deform when the glacier reached an elevation of approximately 180–220 m at each location. This elevation range marks the onset of visible slope deformation. Additionally, the movement and deformation of the Portage slope started before the glacier terminus retreated beyond the landslide toe (Figures 4 and 7). This indicates that glacier thinning (vertical ice loss), rather than more commonly discussed glacier retreat (lateral reduction in extent), is a crucial factor in providing buttress support. This also highlights how local glacier behavior, particularly non-uniform thinning, drives differential slope responses.

Similar observations have been obtained in other regions in the world where glacier thinning has led to similar patterns of slope acceleration and failure, such as in the Alps (e.g., Great Aletsch Glacier; Kos et al. (2016) and Marzellkamm rock slide; Rechberger et al. (2021)), in Iceland (e.g., Tungnakvíslarjökull area; Lacroix et al. (2022)), and Southern Alps of New Zealand (e.g., Mt Fletcher; McSaveney (2002)). In these cases, the timing of slope failure is closely associated with changes in glacier thickness, with the observed data showing that a critical glacier thickness plays a key role.

5.3. Progressive Failure in Structurally Controlled Paraglacial Rock Slopes

In paraglacial environments, slope failures are commonly progressive failure mechanisms, with slope failures occurring in stages or delayed, sometimes decades to centuries after initial deglaciation (e.g., Ballantyne et al., 2014; Spreafico et al., 2021). In structurally controlled slopes, such failures commonly evolve under subcritical stress conditions, where long-term degradation of rock mass strength occurs through crack propagation or weakening along pre-existing discontinuities.

The up-glacier lateral progression of the unstable area at Portage Glacier is associated with the local evolution of glacier thinning, providing kinematic freedom to the rock mass to deform according to their structural settings, provided that shear stresses exceed the shear resistance of these structures. At Portage B, glacier thinning reached a critical threshold before Portage A. Persistent and ubiquitous J2 fractures (i.e., with a strike sub-parallel to the displacement direction) provide the necessary lateral release planes and degree of freedom (Figure 15a). The latter leads to lateral unloading mainly along J2 fractures providing additional kinematic freedom for the rock slopes located up-glacier, and thus contributes to lateral failure progression toward Portage A. This lateral, up-glacier progression of deformation appears to be a feature that, to our knowledge, has not been previously documented in the literature.

Few hundred meters further up-glacier, significant variations in structural features are observed with the presence of fold structures (e.g., Figure 8f) and less fracturing. These variations likely influence where instabilities develop, and could, in this case, limit further up-glacier progression of the instabilities.

The site-specific behavior aligns with early insights by Bovis (1982), who noted that, although glacier-induced stress changes affect all glaciated valleys, significant slope deformations are unevenly distributed and largely site-specific, governed by local lithology, structural features, and the extent of ice loss. Subsequent studies (Ben-Yehoshua et al., 2025; McSaveney, 2002) also emphasized that glacier thinning unloading the slope toe and structural pre-conditioning are both necessary conditions for large-scale slope failure. The Portage case provides a

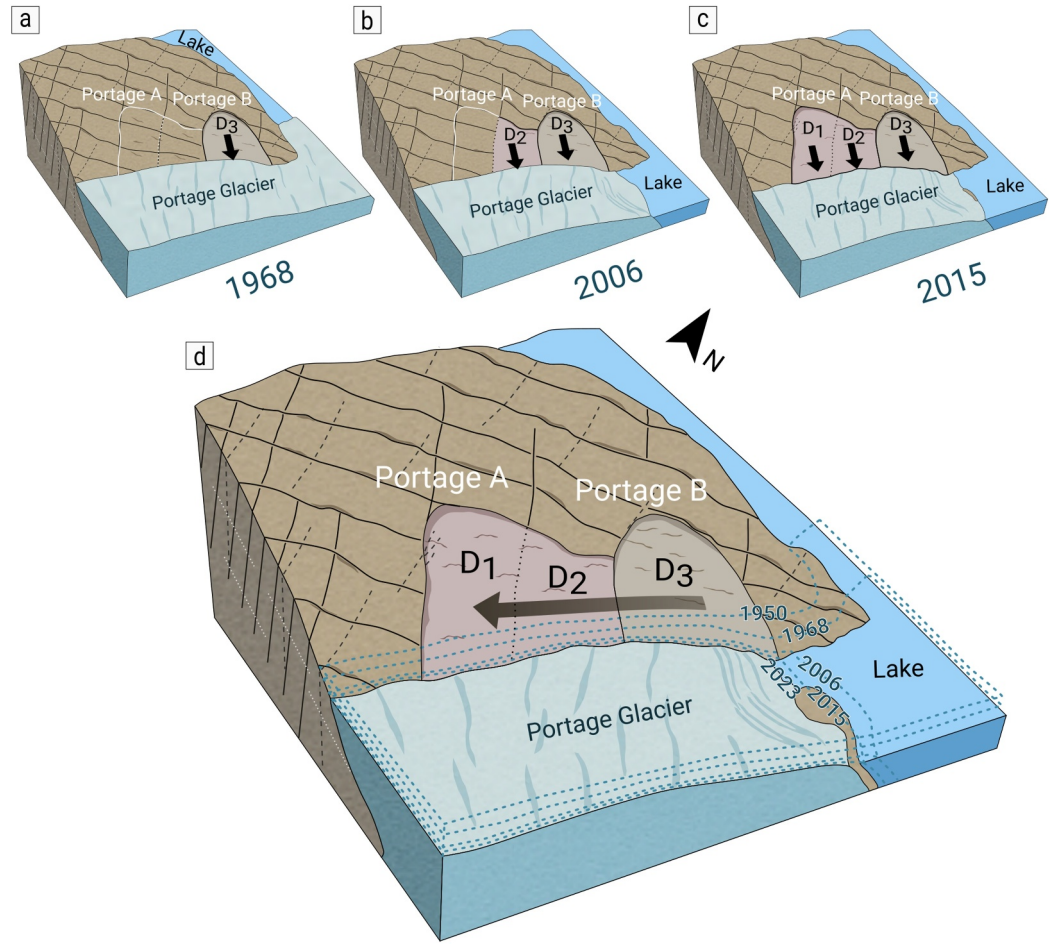

Figure 15. Conceptual sketches illustrating the progressive spatial slope deformation at Portage over time: (a) 1968, (b) 2006, and (c) 2015. (d) Overview conceptual model showing the kinematic evolution of the instabilities over time, highlighting the progressive up-glacier spatial extension in relation to glacier height levels and key structural discontinuities.

detailed example of how glacier thinning can alter mechanical boundary conditions and trigger progressive slope deformation in time and space controlled by pre-existing geological structures.

Beyond the glacier-related processes, our study further highlights the role of additional external drivers, such as seismic activity and precipitation, in contributing to temporal progressive failure. Many paraglacial environments, including the Portage slope, are situated in seismically active regions. The studied slope withstood the 1964 Mw 9.2 Alaska earthquake without immediate large-scale movement. The slope above Portage Glacier exhibited significant slope response only several years later, mirroring delayed responses observed at other paraglacial sites such as Grewingk Glacier (Lemaire et al., 2024) and Fels Glacier (Donati et al., 2023). Seismic shaking can contribute to a reduction in rock mass strength by crack propagation, altering stress fields, and reducing cohesion along existing discontinuities. While earthquakes can act as triggers, they can also serve as preparatory factors, where the full expression of the induced damages in the slope only manifests much later as paraglacial slopes continue to adjust. This highlights the importance of considering delayed, cumulative processes, and multi-driver responses when assessing hazards in these settings.

Additionally, the area around Portage is subject to high precipitation, and the slope shows both seasonal trends and short-term responses to some rainfall events (Figure 13), likely through increases in pore-water pressures that reduce effective stress along pre-existing planes of weakness. This response additionally underscores the importance of hydrological forcing as a contributing factor in progressive slope instability. Understanding the cumulative processes that govern slope responses, including those triggered by rainfall, is essential for anticipating future hazards in paraglacial environments.

The Portage Glacier case exemplifies both temporal and spatial modes of progressive failure in a paraglacial setting. Slope deformation initiated gradually in response to long-term glacier thinning and retreat, combined with external environmental factors such as seismic activity and precipitation, which likely weakened the rock mass strength. As the glacier continued to thin, reducing buttressing and providing kinematic freedom along structural discontinuities, deformation gradually extended laterally up-glacier (spatial progressive failure; Figure 15).

Given the site-specific complexities and the diverse range of contributing factors observed at Portage, it is evident that a nuanced and comprehensive approach is essential for understanding paraglacial slope instability. While regional-scale remote sensing studies are essential for identifying broad patterns, they often miss the more detailed processes that drive slope behavior. For example, the deformation at Portage A was underestimated in a regional analysis covering Prince William Sound (Schaefer et al., 2024), reinforcing the need for detailed satellite- and ground-based assessments to fully capture the complexity of slope evolution in paraglacial settings. Additionally, the Portage case demonstrates the value of multitemporal and multidisciplinary investigations, integrating structural geology, kinematics, rainfall, and long-term monitoring. The value of such multi-sensor approaches, and their contribution to holistic understanding of landslide dynamics, has also been highlighted at the nearby Barry Arm landslide (Schaefer et al., 2023).

6. Conclusions

This study provides a detailed analysis of the progressive up-glacier slope deformation at Portage Glacier. The slope instability reflects a complex interaction of factors, including structural geology, glacier thinning, seismic activity, and meteorological influences. We identified three kinematic domains (D1, D2, and D3) with distinct yet interconnected movement patterns driven by structural discontinuities and glacial dynamics. While D1 and D2, within Portage A, exhibit rapid and variable displacement rates (from ~0.09 m/year to >2 m/year), D3, within Portage B, experiences slower and rather uniform movement.

Failure of the Portage slope started when the glacier reached a critical thickness threshold, indicating that debuttressing played a crucial role in destabilization. This initiation of slope deformation coincided with glacier thinning at elevations of 180–220 m a.s.l., where reduced glacial support enabled deep-seated translational sliding. This provided the rock mass with the necessary kinematic freedom to deform and expand laterally up-glaciers, controlled by structural discontinuities. The variations in structural features in the slope, including fold structures and reduced fracturing, may limit the development of large-scale deep-seated instability up-glaciers. These observations contribute to a growing body of evidence emphasizing that structural preconditioning remains a key factor modulating paraglacial rock slope dynamics and failure timing. In this case, glacial thinning is necessary but not sufficient for failure initiation, pointing instead to a critical combination of structural discontinuities and other external influences. This research provides important insights into the processes driving Portage slope instability and offers a solid foundation for future monitoring efforts and risk assessment.

Conflict of Interest

The authors declare no conflicts of interest relevant to this study.

Data Availability Statement

The SfM-derived DEMs from 2022 and 2023 are available from Lemaire (2024), https://doi.org/10.5281/zenodo.14548600.

Acknowledgments
This project was funded by the Deutsche Forschungsgemeinschaft (DFG, German Research Foundation—447808231). We would like to thank the associate editor and the reviewers for their valuable comments and suggestions, which greatly helped improve this manuscript. Open Access funding enabled and organized by Projekt DEAL.

References

Agisoft Metashape. (2022). Agisoft metashape (version 1.8.5).

Agliardi, F., Crosta, G. B., Meloni, F., Valle, C., & Rivolta, C. (2013). Structurally-controlled instability, damage and slope failure in a porphyry rock mass. *Tectonophysics*, *605*, 34–47. https://doi.org/10.1016/j.tecto.2013.05.033

Augustinus, P. C. (1995). Rock mass strength and the stability of some glacial valley slopes. *Zeitschrift für Geomorphologie*, *39*(1), 55–68. https://doi.org/10.1127/zfg/39/1995/55

Ballantyne, C. K. (2002). Paraglacial geomorphology. *Quaternary Science Reviews*, *21*(18–19), 1935–2017. https://doi.org/10.1016/S0277-3791(02)00005-7

Ballantyne, C. K., Sandeman, G. F., Stone, J. O., & Wilson, P. (2014). Rock-slope failure following late Pleistocene deglaciation on tectonically stable mountainous terrain. *Quaternary Science Reviews*, *86*, 144–157. https://doi.org/10.1016/j.quascirev.2013.12.021

Bamler, R., & Hartl, P. (1998). Synthetic aperture radar interferometry. *Inverse Problems*, *14*(4), R1–R54. https://doi.org/10.1088/0266-5611/14/4/001

Barnes, F. F. (1943). Geology of the portage pass area, Alaska. *US Geological Survey Bulletin*, *926-D*, 211–235.

Benn, D. I., Warren, C. R., & Mottram, R. H. (2007). Calving processes and the dynamics of calving glaciers. *Earth-Science Reviews*, *82*(3), 143–179. https://doi.org/10.1016/j.earscirev.2007.02.002

Ben-Yehoshua, D., Erlingsson, S., Sæmundsson, Þ., Hermanns, R. L., Magnússon, E., Askew, R. A., & Helgason, J. (2025). The destabilizing effect of glacial unloading on a large volcanic slope instability in Southeast Iceland. *GeoHazards*, *6*(1), 1. https://doi.org/10.3390/geohazards6010001

Ben-Yehoshua, D., Sæmundsson, Þ., Helgason, J. K., Belart, J. M. C., Sigurðsson, J. V., & Erlingsson, S. (2022). Paraglacial exposure and collapse of glacial sediment: The 2013 landslide onto Svínafellsjökull, southeast Iceland. *Earth Surface Processes and Landforms*, *47*(10), 2612–2627. https://doi.org/10.1002/esp.5398

Blaber, J., Adair, B., & Antoniou, A. (2015). Ncorr: Open-source 2D digital image correlation matlab software. *Experimental Mechanics*, *55*(6), 1105–1122. https://doi.org/10.1007/s11340-015-0009-1

Blaber, J., & Antoniou, A. (2017). Ncorr: Instruction manual.

Bovis, M. J. (1982). Uphill-facing (antislope) scarps in the coast mountains, southwest British Columbia. *Geological Society of America Bulletin*, *93*(8), 804. https://doi.org/10.1130/0016-7606(1982)93<804:uasitc>2.0.co;2

Brown, J., Ferrians, O. J., Jr., Heginbottom, J. A., & Melnikov, E. S. (1997). *Circum-arctic map of permafrost and ground-ice conditions*. U.S. Geological Survey.

Chen, H., & Lee, C. F. (2003). A dynamic model for rainfall-induced landslides on natural slopes. *Geomorphology*, *51*(4), 269–288. https://doi.org/10.1016/S0169-555X(02)00224-6

CloudCompare. (2023). CloudCompare 32.12 [GPL Software]. Retrieved from https://www.cloudcompare.org/

Cody, E., Draebing, D., McColl, S., Cook, S., & Brideau, M.-A. (2020). Geomorphology and geological controls of an active paraglacial rockslide in the New Zealand Southern Alps. *Landslides*, *17*(4), 755–776. https://doi.org/10.1007/s10346-019-01316-2

Coe, J. A., Bessette-Kirton, E. K., & Geertsema, M. (2018). Increasing rock-avalanche size and mobility in Glacier Bay National park and preserve, Alaska detected from 1984 to 2016 landsat imagery. *Landslides*, *15*(3), 393–407. https://doi.org/10.1007/s10346-017-0879-7

Crossen, K. (2007). Portage glacier and portage pass, Alaska: Little Ice age dynamics and the chronology of glacial retreat. *Polar Geography*, *30*(3), 107–138. https://doi.org/10.1080/10889370701742787

Dahal, R. K., & Hasegawa, S. (2008). Representative rainfall thresholds for landslides in the Nepal Himalaya. *Geomorphology*, *100*(3), 429–443. https://doi.org/10.1016/j.geomorph.2008.01.014

Dai, C., Higman, B., Lynett, P. J., Jacquemart, M., Howat, I. M., Liljedahl, A. K., et al. (2020). Detection and assessment of a large and potentially tsunamigenic periglacial landslide in Barry arm, Alaska. *Geophysical Research Letters*, *47*(22), e2020GL089800. https://doi.org/10.1029/2020GL089800

Darrow, M. M., Daanen, R. P., & Gould, M. C. (2024). Documenting the collision of a landslide in Permafrost with a highway embankment. *Environmental and Engineering Geoscience*, *30*(1–2), 1–18. https://doi.org/10.21663/EEG-D-23-00080

Deline, P., Gruber, S., Delaloye, R., Fischer, L., Geertsema, M., Giardino, M., et al. (2015). Ice loss and slope stability in high-mountain regions. In *Snow and ice-related hazards, risks, and disasters* (pp. 521–561). Elsevier. https://doi.org/10.1016/B978-0-12-394849-6.00015-9

Dini, B., Manconi, A., & Loew, S. (2019). Investigation of slope instabilities in NW Bhutan as derived from systematic DInSAR analyses. *Engineering Geology*, *259*, 105111. https://doi.org/10.1016/j.enggeo.2019.04.008

Donati, D., Stead, D., Rabus, B., Engelbrecht, J., Clague, J., Newman, S., & Mirko, F. (2023). Characterization of the fels landslide (Alaska) using combined terrestrial, aerial, and satellite remote sensing data. *Remote Sensing*, *16*(1), 117. https://doi.org/10.3390/rs16010117

Dufresne, A., Wolken, G. J., Hibert, C., Bessette-Kirton, E. K., Coe, J. A., Geertsema, M., & Ekström, G. (2019). The 2016 Lamplugh rock avalanche, Alaska: Deposit structures and emplacement dynamics. *Landslides*, *16*(12), 2301–2319. https://doi.org/10.1007/s10346-019-01225-4

Eberhardt, E., Stead, D., & Loew, S. (2017). Progressive failure, rock mass fatigue and early warning applied to deep-seated rock slope failures. In *Presented at the ISRM progressive rock failure conference, ascona, Switzerland*.

Etzelmüller, B., Czekirda, J., Magnin, F., Duvillard, P.-A., Ravanel, L., Malet, E., et al. (2022). Permafrost in monitored unstable rock slopes in Norway – New insights from temperature and surface velocity measurements, geophysical surveying, and ground temperature modelling. *Earth Surface Dynamics*, *10*(1), 97–129. https://doi.org/10.5194/esurf-10-97-2022

Evans, S. G., & Clague, J. J. (1994). Recent climatic change and catastrophic geomorphic processes in mountain environments. *Geomorphology*, *10*(1–4), 107–128. https://doi.org/10.1016/0169-555X(94)90011-6

Ferrians, O. J., Jr. (1965). *Permafrost map of Alaska*. U.S. Geological Survey. Retrieved from https://dggs.alaska.gov/pubs/id/13619

U.S. Geological Survey. (2020). M 9.2 - 1964 Prince William sound earthquake, Alaska. Retrieved from https://earthquake.usgs.gov/earthquakes/eventpage/iscgem869809/shakemap/intensity

Glueer, F., Loew, S., & Manconi, A. (2020). Paraglacial history and structure of the Moosfluh landslide (1850–2016), Switzerland. *Geomorphology*, *355*, 106677. https://doi.org/10.1016/j.geomorph.2019.02.021

Goodman, R. E. (1989). *Introduction to rock mechanics* (2nd ed.). New York: Wiley.

Gorum, T., Fan, X., van Westen, C. J., Huang, R. Q., Xu, Q., Tang, C., & Wang, G. (2011). Distribution pattern of earthquake-induced landslides triggered by the 12 May 2008 Wenchuan earthquake. *Geomorphology*, *133*(3–4), 152–167. https://doi.org/10.1016/j.geomorph.2010.12.030

Grämiger, L. M., Moore, J. R., Gischig, V. S., Ivy-Ochs, S., & Loew, S. (2017). Beyond debuttressing: Mechanics of paraglacial rock slope damage during repeat glacial cycles: Paraglacial rock slope mechanics. *Journal of Geophysical Research: Earth Surface*, *122*(4), 1004–1036. https://doi.org/10.1002/2016JF003967

Higman, B., Shugar, D. H., Stark, C. P., Ekström, G., Koppes, M. N., Lynett, P., et al. (2018). The 2015 landslide and tsunami in Taan Fiord, Alaska. *Scientific Reports*, *8*(1), 12993. https://doi.org/10.1038/s41598-018-30475-w

Hugentobler, M., Aaron, J., Loew, S., & Roques, C. (2022). Hydro-mechanical interactions of a rock slope with a retreating temperate valley glacier. *Journal of Geophysical Research: Earth Surface*, *127*(4), e2021JF006484. https://doi.org/10.1029/2021JF006484

Huggel, C., Clague, J. J., & Korup, O. (2012). Is climate change responsible for changing landslide activity in high mountains? Climate change and landslides in high mountains. *Earth Surface Processes and Landforms*, *37*(1), 77–91. https://doi.org/10.1002/esp.2223

Huggel, C., Fischer, L., Schneider, D., & Haeberli, W. (2010). Research advances on climate-induced slope instability in glacier and permafrost high-mountain environments. *Geographica Helvetica*, *65*(2), 146–156. https://doi.org/10.5194/gh-65-146-2010

Hugonnet, R., McNabb, R., Berthier, E., Menounos, B., Nuth, C., Girod, L., et al. (2021). Accelerated global glacier mass loss in the early twenty-first century. *Nature*, *592*(7856), 726–731. https://doi.org/10.1038/s41586-021-03436-z

Hungr, O., Leroueil, S., & Picarelli, L. (2014). The varnes classification of landslide types, an update. *Landslides*, *11*(2), 167–194. https://doi.org/10.1007/s10346-013-0436-y

Iverson, R. M. (2000). Landslide triggering by rain infiltration. *Water Resources Research*, *36*(7), 1897–1910. https://doi.org/10.1029/2000WR900090

Jacquemart, M. (2020). mjacqu/FlatCreekProject: Release linked to GSA geology publication (version v1.0.0). *Zenodo*. https://doi.org/10.5281/ZENODO.3727304

Jacquemart, M., & Tiampo, K. (2021). Leveraging time series analysis of radar coherence and normalized difference vegetation index ratios to characterize pre-failure activity of the mud creek landslide, California. *Natural Hazards and Earth System Sciences*, *21*(2), 629–642. https://doi.org/10.5194/nhess-21-629-2021

Jones, N., Manconi, A., & Strom, A. (2021). Active landslides in the Rogun catchment, Tajikistan, and their river damming hazard potential. *Landslides*, *18*(11), 3599–3613. https://doi.org/10.1007/s10346-021-01706-5

Jorgenson, M., Yoshikawa, K., Kanevskiy, M., Shur, Y., Romanovsky, V., Marchenko, S., & Jones, B. (2008). Permafrost characteristics of Alaska. In *Proceedings of the ninth international conference on permafrost* (Vol. 3, pp. 121–122). University of Alaska.

Keefer, D. K. (1984). Landslides caused by earthquakes. *Geological Society of America Bulletin*, *95*(4), 406. https://doi.org/10.1130/0016-7606(1984)95<406:LCBE>2.0.CO;2

Kennedy, B. W., Trabant, D. C., & Mayo, L. R. (2006). *A century of retreat at portage glacier, south-central Alaska (fact sheet 2006-3141)*. U.S. Geological Survey.

Klimeš, J., Novotný, J., Rapre, A. C., Balek, J., Zahradníček, P., Strozzi, T., et al. (2021). Paraglacial rock slope stability under changing environmental conditions, safuna Lakes, Cordillera Blanca Peru. *Frontiers in Earth Science*, *9*, 607277. https://doi.org/10.3389/feart.2021.607277

Kos, A., Amann, F., Strozzi, T., Delaloye, R., Ruette, J., & Springman, S. (2016). Contemporary glacier retreat triggers a rapid landslide response, great aletsch glacier, Switzerland. *Geophysical Research Letters*, *43*(24), 12466–12474. https://doi.org/10.1002/2016GL071708

Lacroix, P., Belart, J. M. C., Berthier, E., Sæmundsson, Þ., & Jónsdóttir, K. (2022). Mechanisms of landslide destabilization induced by glacier-retreat on tungnakvíslarjökull area, Iceland. *Geophysical Research Letters*, *49*(14), e2022GL098302. https://doi.org/10.1029/2022GL098302

Lemaire, E. (2024). Portage slope 2022 and 2023 DEMs [Dataset]. *Zenodo*. https://doi.org/10.5281/ZENODO.14548600

Lemaire, E., Dufresne, A., Hamdi, P., Higman, B., Wolken, G. J., & Amann, F. (2024). Back-analysis of the paraglacial slope failure at Grewingk glacier and Lake, Alaska. *Landslides*, *21*(4), 775–789. https://doi.org/10.1007/s10346-023-02177-6

Lemaire, E., Mreyen, A.-S., Dufresne, A., & Havenith, H.-B. (2020). Analysis of the influence of structural geology on the massive seismic slope failure potential supported by numerical modelling. *Geosciences*, *10*(8), 323. https://doi.org/10.3390/geosciences10080323

Li, J., Abers, G. A., Kim, Y., & Christensen, D. (2013). Alaska megathrust 1: Seismicity 43 years after the great 1964 Alaska megathrust earthquake: Alaska megathrust 1. *Journal of Geophysical Research: Solid Earth*, *118*(9), 4861–4871. https://doi.org/10.1002/jgrb.50358

Manconi, A. (2021). How phase aliasing limits systematic space-borne DInSAR monitoring and failure forecast of alpine landslides. *Engineering Geology*, *287*, 106094. https://doi.org/10.1016/j.enggeo.2021.106094

Manconi, A., Jones, N., Loew, S., Strozzi, T., Caduff, R., & Wegmueller, U. (2024). Monitoring surface deformation with spaceborne radar interferometry in landslide complexes: Insights from the Brienz/Brinzauls slope instability, Swiss Alps. *Landslides*, *21*(10), 2519–2533. https://doi.org/10.1007/s10346-024-02291-z

Marc, O., Hovius, N., Meunier, P., Uchida, T., & Hayashi, S. (2015). Transient changes of landslide rates after earthquakes. *Geology*, *43*(10), 883–886. https://doi.org/10.1130/G36961.1

Markland, J. T. (1972). *A useful technique for estimating the stability of rock slopes when the rigid wedge slide type type of failure is expected*. Imperial College of Science and Technology.

Mayo, L. R., Zenone, C., & Trabant, D. (1977). *Reconnaissance hydrology of portage glacier basin, Alaska (No. 583). Hydrologic Atlas*. U.S. Geological Survey. https://doi.org/10.3133/ha583

McColl, S. T. (2012). Paraglacial rock-slope stability. *Geomorphology*, *153–154*, 1–16. https://doi.org/10.1016/j.geomorph.2012.02.015

McColl, S. T., Davies, T., & McSaveney, M. (2010). Glacier retreat and rock-slope stability: Debunking debuttressing. In *Presented at the geologically active: Delegate papers 11th congress of the international association for engineering geology and the environment, Auckland, aotearoa*.

McColl, S. T., & Davies, T. R. H. (2013). Large ice-contact slope movements: Glacial buttressing, deformation and erosion. *Earth Surface Processes and Landforms*, *38*(10), 1102–1115. https://doi.org/10.1002/esp.3346

McSaveney, M. J. (2002). Recent rockfalls and rock avalanches in Mount Cook national park, New Zealand. In *Reviews in engineering geology* (Vol. 15, pp. 35–70). Geological Society of America. https://doi.org/10.1130/REG15-p35

Miles, E. S., Watson, C. S., Brun, F., Berthier, E., Esteves, M., Quincey, D. J., et al. (2018). Ablative and geomorphic effects of a supraglacial lake drainage and outburst event, Nepal Himalaya. https://doi.org/10.5194/tc-2018-152

Miller, D. J. (1960). Giant waves in Lituya Bay Alaska. In *Geological Survey professional paper 354-C*.

Muñoz-Sabater, J., Dutra, E., Agustí-Panareda, A., Albergel, C., Arduini, G., Balsamo, G., et al. (2021). ERA5-Land: A state-of-the-art global reanalysis dataset for land applications. *Earth System Science Data*, *13*(9), 4349–4383. https://doi.org/10.5194/essd-13-4349-2021

National Weather Service. (2024). Portage, portage glacier [Dataset]. Retrieved from https://www.weather.gov/wrh/timeseries?site=PATO

Nistor, M., & Petcu, M. I. (2014). *The role of glaciers in the evolution of Prince William Sound landscape ecosystems, Alaska* (Vol. 59). STUDIA UBB AMBIENTUM.

OCM Partners. (2015). 2015 lidar: Municipality of Anchorage, AK. NOAA national centers for environmental information,. Retrieved from https://www.fisheries.noaa.gov/inport/item/50281

Oppikofer, T., Jaboyedoff, M., & Keusen, H.-R. (2008). Collapse at the eastern Eiger flank in the Swiss Alps. *Nature Geoscience*, *1*(8), 531–535. https://doi.org/10.1038/ngeo258

Pastick, N. J., Jorgenson, M. T., Wylie, B. K., Nield, S. J., Johnson, K. D., & Finley, A. O. (2015). Distribution of near-surface permafrost in Alaska: Estimates of present and future conditions. *Remote Sensing of Environment*, *168*, 301–315. https://doi.org/10.1016/j.rse.2015.07.019

Patton, A. I., Rathburn, S. L., Capps, D. M., McGrath, D., & Brown, R. A. (2021). Ongoing landslide deformation in thawing permafrost. *Geophysical Research Letters*, *48*(16), e2021GL092959. https://doi.org/10.1029/2021GL092959

Petley, D. (2022). The 17 September 2022 rock avalanche at Lamplugh glacier in Alaska. Retrieved from https://blogs.agu.org/landslideblog/2022/09/23/lamplugh-glacier-1/

Rechberger, C., Fey, C., & Zangerl, C. (2021). Structural characterisation, internal deformation, and kinematics of an active deep-seated rock slide in a valley glacier retreat area. *Engineering Geology*, *286*, 106048. https://doi.org/10.1016/j.enggeo.2021.106048

Riva, F., Agliardi, F., Amitrano, D., & Crosta, G. (2018). Damage-based time-dependent modeling of paraglacial to postglacial progressive failure of large rock slopes. *Journal of Geophysical Research: Earth Surface*, *123*(1), 124–141. https://doi.org/10.1002/2017JF004423

Schaefer, L. N., Coe, J. A., Wikstrom Jones, K., Collins, B. D., Staley, D. M., West, M., et al. (2023). Kinematic evolution of a large paraglacial landslide in the barry arm fjord of Alaska. *Journal of Geophysical Research: Earth Surface*, *128*(11), e2023JF007119. https://doi.org/10.1029/2023JF007119

Schaefer, L. N., Kim, J., Staley, D. M., Lu, Z., & Barnhart, K. R. (2024). *Satellite interferometry landslide detection and preliminary tsunamigenic plausibility assessment in Prince William Sound, southcentral Alaska (no. 2023–1099)*. Open-File Report. U.S. Geological Survey. https://doi.org/10.3133/ofr20231099

Sepúlveda, S., Tobar, C., Rosales, V., Ochoa-Cornejo, F., & Lara, M. (2023). Megalandslides and deglaciation: Modelling of two case studies in the central Andes. *Natural Hazards*, *118*, 1–12. https://doi.org/10.1007/s11069-023-06067-x

Slaymaker, O. (2009). The future of geomorphology: The future of geomorphology. *Geography Compass*, *3*(1), 329–349. https://doi.org/10.1111/j.1749-8198.2008.00178.x

Spreafico, M. C., Sternai, P., & Agliardi, F. (2021). Paraglacial rock-slope deformations: Sudden or delayed response? Insights from an integrated numerical modelling approach. *Landslides*, *18*(4), 1311–1326. https://doi.org/10.1007/s10346-020-01560-x

Stead, D., & Wolter, A. (2015). A critical review of rock slope failure mechanisms: The importance of structural geology. *Journal of Structural Geology*, *74*, 1–23. https://doi.org/10.1016/j.jsg.2015.02.002

Storni, E., Hugentobler, M., Manconi, A., & Loew, S. (2020). Monitoring and analysis of active rockslide-glacier interactions (Moosfluh, Switzerland). *Geomorphology*, *371*, 107414. https://doi.org/10.1016/j.geomorph.2020.107414

Strozzi, T., Caduff, R., Jones, N., Barboux, C., Delaloye, R., Bodin, X., et al. (2020). Monitoring rock glacier kinematics with satellite synthetic aperture radar. *Remote Sensing*, *12*(3), 559. https://doi.org/10.3390/rs12030559

Strozzi, T., Klimeš, J., Frey, H., Caduff, R., Huggel, C., Wegmüller, U., & Rapre, A. C. (2018). Satellite SAR interferometry for the improved assessment of the state of activity of landslides: A case study from the cordilleras of Peru. *Remote Sensing of Environment*, *217*, 111–125. https://doi.org/10.1016/j.rse.2018.08.014

U.S. Geological Survey. (2024). Search earthquake catalog. Retrieved from https://earthquake.usgs.gov/earthquakes/search/

Vick, L. M., Böhme, M., Rouyet, L., Bergh, S. G., Corner, G. D., & Lauknes, T. R. (2020). Structurally controlled rock slope deformation in northern Norway. *Landslides*, *17*(8), 1745–1776. https://doi.org/10.1007/s10346-020-01421-7

Voigtländer, A. (2020). *Controls on progressive rock failure: Environmental conditions, subcritical mechanisms and rock stress memory*. (PhD Thesis). Technical University of Munich.

Walden, J., Jacquemart, M., Higman, B., Hugonnet, R., Manconi, A., & Farinotti, D. (2025). Landslide activation during deglaciation in a fjord-dominated landscape: Observations from southern Alaska (1984–2022). *Natural Hazards and Earth System Sciences*, *25*(6), 2045–2073. https://doi.org/10.5194/nhess-25-2045-2025

Wasowski, J., & Bovenga, F. (2014). Investigating landslides and unstable slopes with satellite multi temporal interferometry: Current issues and future perspectives. *Engineering Geology*, *174*, 103–138. https://doi.org/10.1016/j.enggeo.2014.03.003

Wegnüller, U., Werner, C., Strozzi, T., Wiesmann, A., Frey, O., & Santoro, M. (2016). Sentinel-1 support in the GAMMA software. *Procedia Computer Science*, *100*, 1305–1312. https://doi.org/10.1016/j.procs.2016.09.246

Wiles, G. C., & Calkin, P. E. (1992). Reconstruction of a debris-slide-initiated flood in the southern Kenai Mountains, Alaska. *Geomorphology*, *5*(6), 535–546. https://doi.org/10.1016/0169-555X(92)90024-I

Wyllie, D. C., & Mah, C. W. (2004). *Rock slope engineering: Civil and mining* (4th ed.). CRC Press. https://doi.org/10.1201/9781315274980

Wyllie, D. C., & Norrish, N. I. (1996). Landslides: Investigation and mitigation. In *Chapter 14-Rock strength properties and their measurement* (Vol. 247). Transportation Research Board Special Report. Retrieved from https://trid.trb.org/view/462512

Zechmann, J. M., Wikstrom Jones, K. M., & Wolken, G. J. (2024). *Lidar-derived elevation data for portage, southcentral Alaska, collected October 15, 2020 (no. RDF 2024-7)*. Alaska Division of Geological & Geophysical Surveys. https://doi.org/10.14509/31160

Zhong, Y., Liu, Q., Westoby, M., Nie, Y., Pellicciotti, F., Zhang, B., et al. (2021). Intensified paraglacial slope failures due to accelerating downwasting of a temperate glacier in mt. Gongga, southeastern Tibet Plateau (preprint). *Physical: Geomorphology*. https://doi.org/10.5194/esurf-2021-18